

Benchmarking and Adapting On-Device Large Language Models for Clinical Decision Support

Alif Munim*, Jun Ma*, Omar Ibrahim*, Alhusain Abdalla*, Shuolin Yin, Leo Chen, and Bo Wang

Abstract

Large language models (LLMs) have rapidly advanced in clinical decision-making, yet the deployment of proprietary systems is hindered by privacy concerns and reliance on cloud-based infrastructure. Open-source alternatives allow local inference but often require large model sizes that limit their use in resource-constrained clinical settings. Here, we benchmark two on-device LLMs, gpt-oss-20b and gpt-oss-120b, across three representative clinical tasks: general disease diagnosis, specialty-specific (ophthalmology) diagnosis and management, and simulation of human expert grading and evaluation. We compare their performance with state-of-the-art proprietary models (GPT-5 and o4-mini) and a leading open-source model (DeepSeek-R1), and we further evaluate the adaptability of on-device systems by fine-tuning gpt-oss-20b on general diagnostic data. Across tasks, gpt-oss models achieve performance comparable to or exceeding DeepSeek-R1 and o4-mini despite being substantially smaller. In addition, fine-tuning remarkably improves the diagnostic accuracy of gpt-oss-20b, enabling it to approach the performance of GPT-5. These findings highlight the potential of on-device LLMs to deliver accurate, adaptable, and privacy-preserving clinical decision support, offering a practical pathway for broader integration of LLMs into routine clinical practice.



INTRODUCTION

Large language models (LLMs) are rapidly transforming the landscape of clinical medicine. Trained on massive corpora of general-domain and biomedical text, these models have demonstrated emergent reasoning abilities that enable comprehensive summaries from medical dialogue [1], disease diagnosis, and treatment planning [2]. For example, Med-PaLM [3], [4] and AMIE [5], [6] achieved near-clinician performance in open-ended medical question answering, differential diagnosis, and patient consultation simulations. In real-world evaluations [7], LLM-assisted physicians exhibited improved diagnostic accuracy and management decisions across diverse clinical scenarios. Together, these advances illustrate the growing potential of LLMs to augment clinical expertise and support decision-making at the point of care.

Despite these achievements, the translation of LLMs into real-world clinical workflows remains limited. Most frontier LLMs are proprietary, cloud-hosted, and trained on non-transparent datasets, creating challenges related to data privacy, regulatory compliance, reproducibility, and cost. The transmission of patient information to external servers conflicts with data-governance policies in many health institutions. Moreover, the high cost associated with developing, training, and deploying large-scale proprietary models can be prohibitive for many healthcare institutions.

The open-source community has developed increasingly capable models that approach the performance of proprietary systems while allowing full local control. Models such as DeepSeek-R1 [8] have demonstrated competitive reasoning and clinical comprehension across diagnostic and treatment-related tasks [9], [10]. However, the adoption of DeepSeek-R1 in clinical environments is constrained because of the large model size of 671 billion parameters, which requires substantial computational costs. The models of this scale not only hinder deployment in clinics with limited access to computing resources, but also make fine-tuning for adaptation in evolving clinical domains prohibitively expensive. These limitations underscore the need for smaller, efficient models that retain clinical reasoning ability while remaining feasible for on-premise use.

The recent advancements in on-device LLMs offer a promising solution to the challenges posed by both large proprietary and open-source models. In particular, the gpt-oss family [11] represents this new generation of efficient and privacy-preserving architectures. The gpt-oss-20b model and its larger counterpart, gpt-oss-120b, are designed and optimized for deployment on a single consumer GPU with 16GB and 80GB memory, respectively. This study aims to determine whether on-device LLMs can be practically used for clinical decision support. We systematically benchmark gpt-oss-20b and gpt-oss-120b models across three representative tasks: general disease diagnosis, (ophthalmology) specialty-specific disease

- Alif Munim is with AI Collaborative Centre, University Health Network, Toronto, Canada.
- Jun Ma is with AI Collaborative Centre and Princess Margaret Cancer Centre, University Health Network, Toronto, Canada. (* Equal Contribution)
- Omar Ibrahim is with AI Collaborative Centre, University Health Network, Toronto, Canada. (* Equal Contribution)
- Alhusain Abdalla is with AI Collaborative Centre, University Health Network, Toronto, Canada. (* Equal Contribution)
- Shuolin Yin is with Department of Electrical and Computer Engineering, University of Toronto, Toronto, Canada.
- Leo Chen is with Division of Urology, Department of Surgery, St. Michael's Hospital, Unity Health Toronto and University of Toronto, Toronto, Canada
- Bo Wang (Corresponding Author) is with Peter Munk Cardiac Centre, University Health Network; Department of Laboratory Medicine and Pathobiology and Department of Computer Science, University of Toronto; Vector Institute, Toronto, Canada. E-mail: bowang@vectorinstitute.ai

diagnosis and management, and simulation of human clinician judgement and evaluation (Fig. 1). To establish a clear performance landscape, we compare these on-device models against leading proprietary models (GPT-5 and o4-mini) and a strong open-source model (DeepSeek-R1).

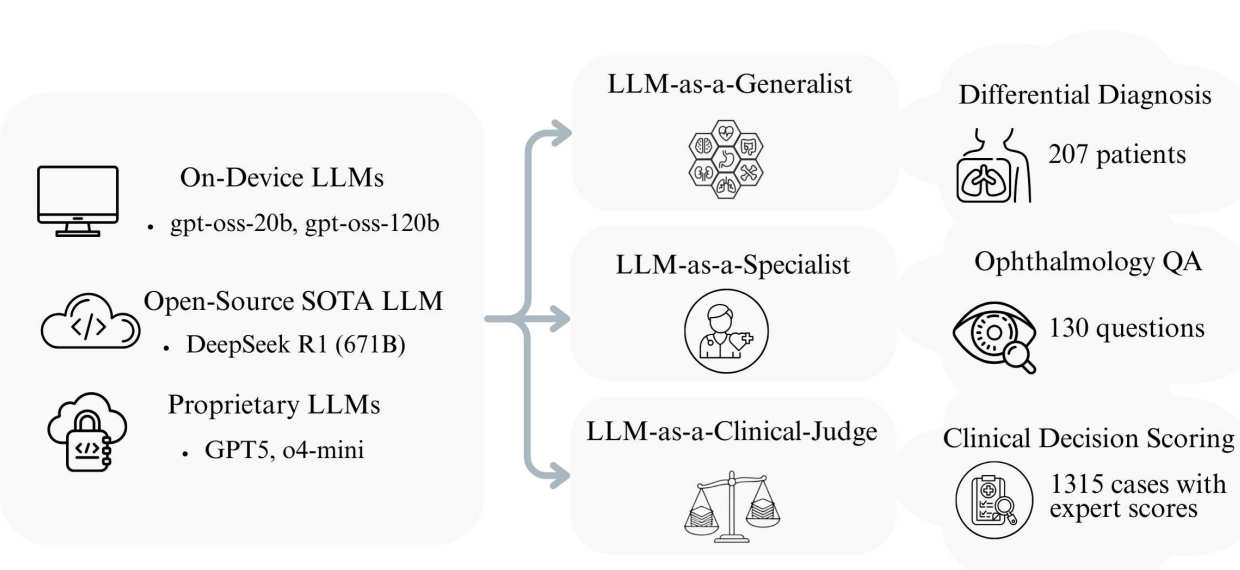


Fig. 1. **Overview of the benchmark framework.** This study compares the on-device LLMs with state-of-the-art open-source and proprietary LLMs across general disease diagnosis, specialty diagnosis and treatment recommendations on ophthalmology multiple-choice questions, and judgment for open-ended clinical decision questions.

RESULTS

Dataset and evaluation methods

We mainly focus on assessing the performance of LLMs on disease diagnosis, treatment recommendations, and simulating expert judgment for open-ended questions, as these are common tasks in clinical practice. We curated three datasets and benchmarked model performance on three scenarios: LLM-as-a-generalist, LLM-as-a-specialist, and LLM-as-a-clinical-judge (Figure 1).

Specifically, to assess the capability of LLMs for general disease diagnosis, we collected 207 case reports from the EuroRAD library where each case contains clinical history, findings from associated medical images (e.g., computed tomography (CT), magnetic resonance imaging (MRI), and ultrasound), and a fine-grained differential diagnosis list (Methods). The task is to select the diagnosis from the list based on patient history and imaging findings (Supplementary Prompt 1).

The second dataset was from a ophthalmology multiple-choice question dataset [12], aiming to evaluate the specialty-specific performance of LLMs (Methods). The dataset contains 39 diagnosis questions and 91 management questions. Each question contains patient sex, age, and examinations findings, such as visual acuity, intraocular pressure, and fundus examinations, and a list of five to nine answer options. The task is to select correct answers, and each question may have multiple correct answers (Supplementary Prompt 2).

The third dataset was adapted from the existing benchmarking study of the DeepSeek-R1 model [10], including 1315 cases with human expert scores from 125 patients across five specialties (internal medicine, neurology, surgery, gynecology, and pediatrics) (Methods). LLMs are tasked to simulate human experts to assess given diagnoses from existing LLMs and assign a score from 1 to 5 based on a predefined rubric. We compare these LLM-generated scores against ground-truth human expert scores (Supplementary Prompt 3-4).

For the LLM-as-a-generalist and LLM-as-a-specialist tasks, the evaluation was based on exact match accuracy. For the LLM-as-a-clinical-judge task, we computed the relative error between the clinicians' scores and the LLM's scores. To ensure rigorous zero-shot evaluation and prevent data leakage, all three benchmark datasets were curated from cases released after the training data cutoff for all evaluated LLMs.

On-device LLMs show competitive zero-shot performance

Fig. 2a compares the diagnostic accuracy of the evaluated models for general disease diagnosis across radiological case reports (Supplementary Table 1). While the proprietary frontier model GPT-5 achieved the highest overall average performance with an accuracy of 88.9% (95% CI: 83.9–92.5%), the on-device models demonstrated strong competitiveness relative to the established baselines. Specifically, the gpt-oss-120b (L) model achieved an average accuracy of 84.1% (95% CI: 78.5–88.4%), effectively matching the efficient proprietary model o4-mini (84.1%; 95% CI: 78.5–86.3%; $p > 0.05$) and

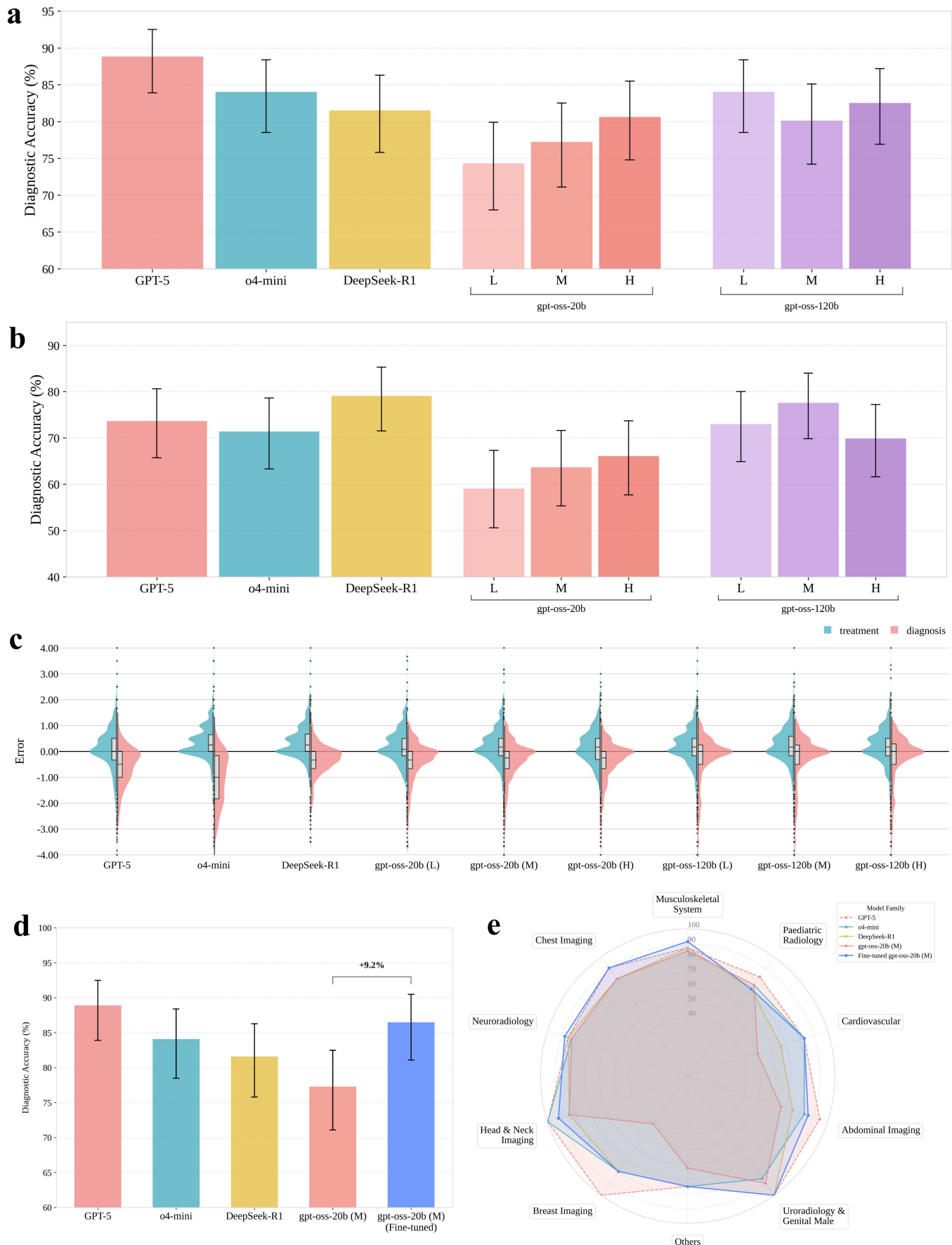


Fig. 2. Zero-shot and fine-tuning performance of on-device LLMs. **a**, Results of LLM-as-a-generalist: diagnosis accuracy on a wide range of radiological cases (N=207). L, M, and H denote low, medium, and high reasoning efforts, respectively. **b**, Results of LLM-as-a-specialist: accuracy on ophthalmology cases (N=130) with diagnosis and management multiple-choice questions. **c**, Results of LLM-as-a-clinical-judge: violin plots comparing the relative error for disease diagnosis and treatment open-ended question assessment (N=1315). **d**, Fine-tuned gpt-oss-20b (M) model outperforms proprietary (o4-mini) and open-source LLMs (DeepSeek-R1) on the disease differential diagnosis task. **e**, Model performance across 10 radiological sub-specialties.

surpassing the leading open-source model DeepSeek-R1 (81.6%; 95% CI: 75.8–86.3%; $p < 0.01$). Furthermore, the highly efficient gpt-oss-20b (H) model secured an accuracy of 80.7% (95% CI: 74.8–85.5%), approaching the performance of the significantly larger DeepSeek-R1 ($p > 0.05$).

Fig. 2b presents the model performance of the LLM-as-a-specialist task on the ophthalmology QA dataset (Supplementary Table 2). The open-source model DeepSeek-R1 achieved the highest overall accuracy of 79.2% (95% CI: 71.5–85.3%), demonstrating particularly strong capabilities in diagnosis (92.3%; 95% CI: 79.7–97.3%) and management (73.6%; 95% CI: 63.7–81.6%). Remarkably, the on-device gpt-oss-120b (M) model secured the second-highest rank with an overall accuracy of 77.7% (95% CI: 69.8–84.0%), surpassing both the proprietary GPT-5 (73.8%; 95% CI: 65.7–80.6%) and o4-mini (71.5%; 95% CI: 63.3–78.6%) baselines ($p < 0.01$). This performance underscores the capacity of locally deployed large models to rival state-of-the-art proprietary systems in specialty-specific medical reasoning. While the smaller gpt-oss-20b variants showed a performance gap, with the best-performing gpt-oss-20b (H) achieving 66.2% (95% CI: 57.7–73.7%), they remained competitive in specific subtasks (e.g., Refractive Disorders or Strabismus). Across all evaluated architectures, models consistently demonstrated higher performance in diagnosis compared to patient management, reflecting the increased complexity of treatment planning in specialty care.

Fig. 2c shows the evaluation results of models acting as clinical judges, measured by the median relative error (interquartile range) between the model's score and human expert consensus. The proprietary GPT-5 achieved the lowest median error for treatment-related judgments (0.00, IQR: -0.33–0.50), demonstrating high alignment with human experts across specialties such as Internal Medicine and Pediatrics. However, for diagnostic assessment, GPT-5 exhibited a tendency to underestimate performance (median error: -0.50, IQR: -1.00–0.00). In contrast, the on-device gpt-oss-120b variants demonstrated high stability, achieving a median error of 0.00 (IQR: -0.50–0.25) across all diagnostic tasks, significantly outperforming o4-mini ($p < 0.01$), which showed a larger deviation (-1.00, IQR: -1.83–0.17). Among the open-source models, DeepSeek-R1 and the gpt-oss-20b series generally aligned well with human scores but displayed slightly higher variability in treatment evaluations compared to the larger 120b models. When stratified by disease frequency, the gpt-oss-120b models maintained consistent accuracy across "Rare", "Less Frequent", and "Frequent" conditions, suggesting that larger on-device models can offer robust, human-aligned evaluation capabilities.

Model reliability was further assessed using standard agreement and stability metrics. Inter-model agreement, measured using Cohen's κ , was moderate for diagnostic reasoning tasks ($\kappa \approx 0.45–0.87$) and lower for treatment evaluation tasks ($\kappa \approx 0.20–0.43$), reflecting the open-ended and subjective nature of clinical management decisions. In contrast, intra-model stability across repeated inference runs was high. For diagnostic judgment tasks, the Intraclass Correlation Coefficient (ICC) indicated excellent reliability across all models (ICC $\approx 0.91–0.97$), while treatment scoring showed greater variability, with proprietary models exhibiting higher stability than open and on-device models. Together, these results support the use of consensus-based aggregation to mitigate stochastic variability and produce reliable clinical outputs.

Fine-tuning substantially improves the diagnostic capability of on-device LLMs

To assess the adaptability of on-device LLMs for clinical decision support, we fine-tuned the gpt-oss-20b (M) model on the general disease diagnosis dataset (Methods). As shown in Fig. 2d (Supplementary Fig. 1–3), the fine-tuned model produced a marked improvement in diagnostic accuracy, increasing from 77.3% (95% CI: 71.1–82.5%) in the base model to 86.5% (95% CI: 81.1–90.5%) after adaptation. This performance not only exceeded the accuracy of DeepSeek-R1 (81.6%, 95% CI: 75.8–86.3%) and o4-mini (84.1%, 95% CI: 78.5–88.4%) but also approached that of the state-of-the-art proprietary GPT-5 model (88.9%, 95% CI: 83.9–92.5%).

To illustrate the impact of fine-tuning on both diagnostic accuracy and reasoning quality, we present three case studies (Supplementary Cases 1–3). Case 1 (Von Hippel-Lindau syndrome) shows fine-tuning enhances reasoning quality even when base models reach correct diagnoses: the base model provided superficial comparisons with uncertain statements, while the fine-tuned model employed systematic multi-system integration with detailed syndrome comparison and definitive synthesis. Cases 2–3 demonstrate error correction through recognition of critical clinical features. Furthermore, the sub-specialty-wise analysis (Fig. 2e, Supplementary Fig. 4) reveals that fine-tuning effectively mitigates domain-specific weaknesses observed in base models, particularly in specialized areas such as cardiovascular and breast imaging.

The substantial performance gain demonstrates that targeted domain adaptation can effectively compensate for the smaller scale of on-device models. Even with medium reasoning effort, the fine-tuned gpt-oss-20b model exhibits diagnostic accuracy comparable to significantly larger proprietary systems while retaining the advantages of local deployability and privacy preservation. These findings highlight the strong potential of lightweight, fine-tuned on-device LLMs to provide high-quality clinical decision support in settings with limited computational resources.

DISCUSSION

This study systematically evaluates the capabilities of on-device large language models across three representative clinical tasks: general diagnosis, specialty-level reasoning, and simulation of expert judgment. Across all settings, the gpt-oss models demonstrate clinically meaningful performance despite their substantially smaller scale relative to frontier proprietary models, underscoring the feasibility of deploying lightweight LLMs directly within healthcare institutions.

In the general disease diagnosis task, on-device models achieved strong zero-shot performance, showing that compact architectures can capture the broad clinical reasoning patterns required for diagnosis. Moreover, in the ophthalmology

specialty task, the on-device gpt-oss-120b model outperformed both GPT-5 and o4-mini while ranking second overall behind DeepSeek-R1. This is noteworthy given that most existing clinical LLM evaluations have focused on large cloud-based models, leaving open the question of whether smaller locally deployable systems can achieve similar levels of generalization. Our findings indicate that modern on-device architectures can support robust performance in common diagnostic scenarios without requiring external computation or data transfer.

The ability of LLMs to act as "clinical judges" is critical for scalable quality assurance and automated evaluation. Our results indicate that on-device models can align closely with human expert consensus, often exhibiting greater stability than efficient proprietary alternatives. This suggests that compact models can support evaluative tasks that require not only factual knowledge but also sensitivity to clinical reasoning standards and rubric-based assessment criteria. This capability is essential for deploying LLMs as automated auditors or second-opinion systems in clinical workflows.

Beyond zero-shot performance, the adaptability of on-device models represents a substantial advantage over closed-source systems. Fine-tuning the gpt-oss-20b model on general diagnosis data substantially improved its performance, even exceeding the diagnostic accuracy of several much larger frontier models. This result suggests that domain-specific optimization can efficiently compensate for smaller model scale. Fine-tuning also enhanced robustness across radiology subspecialties, yielding more uniform performance and mitigating weaknesses observed in the base model. These findings highlight that clinics can deploy efficient, low-cost, customized AI tools tailored to their specific patient demographics and disease prevalences without compromising data privacy.

Taken together, the experiments in this study highlight three key insights. First, compact on-device LLMs can provide strong general diagnostic reasoning and domain-specific performance. Second, on-device LLMs can approximate expert judgment with surprising fidelity, positioning them as valuable components of locally governed AI ecosystems that support both clinical decision-making and meta-evaluative tasks. Third, fine-tuning plays a critical role in achieving competitive accuracy across diverse subspecialties, allowing healthcare institutions to develop tailored high-performing models from relatively small architectures.

Our study also has limitations. First, while our benchmarks cover diagnosis, management, and evaluation, they rely on retrospective patient cases and examination questions, which may not fully capture the complexity and noise of real-time clinical environments. Local deployment mitigates privacy and data governance concerns but introduces operational challenges, including hardware reliability, secure integration with clinical information systems, and ongoing monitoring of model behavior. Fine-tuning requires access to high-quality labeled data, which may be limited in certain specialties.

In summary, this work demonstrates that on-device LLMs offer a promising and practical alternative to large proprietary systems for clinical decision support. These compact models can achieve reliable diagnostic reasoning, robust subspecialty performance, and alignment with expert judgment—all while maintaining strict control over patient data and computational infrastructure. These features position on-device LLMs as strong candidates for safe, scalable, and equitable integration of AI into clinical practice.

METHODS

Dataset curation and pre-processing

Case reports for the LLM-as-a-generalist task were curated from the European Society of Radiology (Eurorad) (<https://www.eurorad.org/>) database across a broad spectrum of subspecialties, including musculoskeletal, cardiovascular, abdominal, uroradiology, neuroradiology, paediatric, head and neck, breast, and chest imaging. To strictly mitigate data leakage, the test set was restricted to cases published in 2025, postdating the training cut-off of the evaluated models. From an initial pool of 350 prospective test cases, we employed GPT-5 to screen and exclude reports containing explicit diagnostic disclosures in the description. Historical cases published prior to 2025 were allocated for fine-tuning, yielding a final dataset comprising 1,895 training cases and 207 independent test cases.

Cases for the LLM-as-a-specialist task were based on the recent ophthalmology multiple-choice question dataset [12]. It contains 130 questions covering six topics: anterior segment diseases, external eye/orbital diseases, glaucoma, ocular trauma, refractive disorders/strabismus, and retinal diseases. Each question has one to six correct answers from five to nine answer choices.

Cases for the LLM-as-a-clinical-judge scoring task were curated from the benchmark data in [10], comprising 125 patient cases. Each case included a chief complaint and up to five diagnostic or treatment recommendations generated by distinct models, including GPT-4, GPT-4o, GPT-3.5, Gem2FTE, and DeepSeek-R1. In this task, the evaluated LLMs were required to audit these predictions by assigning quality scores rather than generating de novo diagnoses. Performance was assessed by measuring the concordance between model-generated scores and reference ratings provided by medical experts.

Task-specific inference protocols

To ensure fair comparison, we developed standardized zero-shot inference pipelines for each clinical task. All protocols utilized a self-consistency framework where each case was queried three independent times ($k = 3$).

General Radiology Diagnosis. The LLM-as-a-generalist diagnostic task was formulated as a constrained single-label selection problem (Supplementary Prompt 1). Models were provided with the patient history and imaging findings and instructed to select the most likely diagnosis strictly verbatim from a provided differential list. Post-processing utilized a deterministic regex-based extractor to isolate the final diagnosis from the generated reasoning stream.

Ophthalmology Specialty QA. The LLM-as-a-specialist task involved complex multiple-choice questions (MCQs) requiring multi-label classification. Unlike the radiology task, models were instructed to “Select ALL correct answers” from options A-Z. The system prompt enforced a strict output format consisting only of concatenated capital letters (e.g., “ABE” or “D”), prohibiting explanatory text in the final output to facilitate automated parsing (Supplementary Prompt 2).

Clinical Judgment Simulation. The LLM-as-a-clinical-judge task evaluated the models’ ability to simulate expert clinical judgment. Models were presented with a clinical case adapted from [10], alongside a candidate diagnosis/treatment plan, and a reference standard. They were instructed to assign a quality score on a 5-point Likert scale (1 = Most relevant options missing, 5 = All relevant options mentioned) based on a strict scoring rubric. Half-point scores (e.g., 4.5) were permitted to capture granular distinctions in quality (Supplementary Prompt 3).

Inference Implementation

We benchmarked three distinct categories of models to represent the current landscape of LLMs:

Proprietary Frontier Models (GPT-5 and o4-mini). We selected the latest snapshots of OpenAI’s premier reasoning models, `gpt-5-2025-08-07` and `o4-mini-2025-04-16`. These models represent the current state-of-the-art in closed-source reasoning, utilizing hidden chain-of-thought (CoT) processing to plan responses before output generation. Inference was conducted via the OpenAI Responses API. To evaluate the impact of inference-time compute, we modulated the `reasoning_effort` parameter (`low`, `medium`, `high`). For all tasks, we utilized the default `medium` effort setting.

Open-Source State-of-the-Art Model (DeepSeek-R1). To represent the pinnacle of open-source capability, we evaluated the 671-billion parameter `DeepSeek-R1-0528`. This model utilizes large-scale reinforcement learning to optimize reasoning paths and is currently the strongest non-proprietary baseline available. Inference was performed via the OpenRouter API. We utilized a context window of 8,192 tokens to strictly enforce the capture of the model’s native reinforcement-learning-aligned reasoning traces.

On-Device Models (gpt-oss-20b and gpt-oss-120b). The primary focus of this study is the `gpt-oss` family, a new generation of efficient, privacy-preserving architectures designed for local deployment. We evaluated both the 20-billion parameter variant (optimized for consumer GPUs) and the 120-billion parameter variant to assess the trade-off between computational efficiency and diagnostic reasoning capability. The `gpt-oss` models were evaluated using the Hugging Face Inference Router, targeting the Fireworks AI provider for the 20b model and Cerebras for the 120b model to maximize throughput. Similar to the proprietary OpenAI models, we modulated the `reasoning_effort` parameter (`low`, `medium`, `high`), in this case through the system prompt (e.g. by appending “Reasoning: high” for the highest level of reasoning) to trigger extended chain-of-thought generation patterns. Output parsing relied on a custom regex extractor to identify valid answer sequences within the generated text.

Training Dataset Preparation for Radiological Cases

`gpt-oss` represents a family of reasoning-capable language models designed to generate structured Chain-of-Thought (CoT) reasoning during inference. To develop high-quality training data for fine-tuning `gpt-oss-20b` on radiological diagnosis tasks, we employed `gpt-oss-120b`—a substantially larger model from the same architectural family—to curate systematic diagnostic reasoning data for all 1,895 cases in the Eurorad dataset. The use of `gpt-oss-120b` for data curation was predicated on three key advantages: (i) architectural consistency between the 120b and 20b variants ensures compatibility of reasoning patterns, (ii) the larger parameter count enables more sophisticated medical reasoning and systematic differential diagnosis evaluation, and (iii) automated generation provides scalable, consistent reasoning data across the entire dataset.

For each radiological case, `gpt-oss-120b` was provided with the clinical case presentation (comprising patient history and imaging findings), the original expert radiologist discussion from the Eurorad dataset as contextual grounding, and the list of differential diagnoses. The original discussion, which provided academic descriptions of case characteristics and imaging findings, served as reference material to inform the generation of improved systematic reasoning. The model was instructed to generate Chain-of-Thought reasoning following a structured four-step diagnostic framework: (1) symptom-finding correlation—establishing connections between clinical presentation and imaging observations, (2) differential mapping—evaluating how imaging findings support or contradict each candidate diagnosis, (3) systematic elimination—providing explicit reasoning for excluding less likely diagnostic options, and (4) diagnostic convergence—demonstrating the logical pathway to the final diagnosis. Reasoning generation employed the following parameters: `temperature = 0.6`, `maximum output tokens = 2000`, `target length = 200–400 words`, accessed via the HuggingFace Inference API.

Generated reasoning samples underwent systematic validation to ensure data quality. We verified that all 1,895 generated reasoning chains converged to the correct ground truth diagnosis, confirming alignment between the model’s reasoning process and the clinically validated diagnoses. Automated quality metrics assessed each response for: (i) appropriate length (200–600 words acceptable range), (ii) presence of all four required reasoning components (symptom-finding correlation, differential mapping, systematic elimination, and diagnostic convergence), and (iii) response completeness (absence of premature truncation). Additionally, a subset of cases was manually inspected to validate that the systematic elimination reasoning across all four reasoning phases logically progressed toward the correct diagnosis, and that the final diagnosis selection matched the ground truth. For this subset, the generated reasoning was also compared against the original discussions to ensure clinical accuracy and logical coherence. The complete dataset comprising all 1,895 cases was used for `gpt-oss-20b` fine-tuning.

Training Protocol

Fine-tuning of gpt-oss-20b (M) was performed using the curated reasoning dataset generated by gpt-oss-120b. The model was loaded using the Unslloth framework with 4-bit quantization to enable efficient training on limited computational resources while maintaining model performance. A maximum sequence length of 4,096 tokens was configured to accommodate the clinical case presentations and associated reasoning chains.

Parameter-efficient fine-tuning was implemented using Low-Rank Adaptation (LoRA) with rank $r=32$ and $\alpha=64$, targeting all linear layers in the model architecture, including query, key, value, and output projections, as well as the feed-forward network components (gate, up, and down projections) across all 32 transformer layers. Additionally, expert layers within the mixture-of-experts architecture were targeted at strategic depths: early layers (0-7) for initial processing, middle layers (8-15) for pattern recognition and reasoning, upper layers (16-23) for deep reasoning, and deep layers (24-31) for final refinement and output generation. This comprehensive targeting strategy ensured that the model could effectively learn diagnostic reasoning patterns at multiple levels of abstraction. A LoRA dropout rate of 0.05 was applied to prevent overfitting, and gradient checkpointing was enabled to reduce memory consumption during training.

The curated reasoning data was formatted using the gpt-oss chat template with medium reasoning effort, incorporating the gpt-oss-120b-generated reasoning as structured thinking content. This approach enabled the model to learn from the systematic diagnostic patterns demonstrated by the larger model while maintaining compatibility with the gpt-oss reasoning framework. Training was conducted over 3 epochs using the AdamW optimizer with a learning rate of 1×10^{-4} , cosine learning rate scheduling, and a warmup ratio of 0.1. Mixed-precision training with bfloat16 was utilized to accelerate computation while maintaining numerical stability. All experiments were conducted with fixed random seeds to ensure reproducibility.

Inference protocol of fine-tuned model

To evaluate the fine-tuned gpt-oss-20b model on radiological diagnosis, we designed a controlled inference pipeline optimized for the exploration of deterministic and diverse hypotheses. All predictions were generated using group beam search, a decoding strategy that encourages exploration across diverse reasoning paths while also maintaining stability in high-stakes clinical settings. After systematic experimentation with different decoding settings, we found that a configuration of 13 beams, 13 beam groups, and a diversity penalty of 0.5 provided the strongest performance on the Eurorad validation set. This setup enforced full beam-group separation, ensuring that each beam starts its own reasoning trajectory and looks at the presented case from a different angle, which is particularly effective in reducing mode collapse and repetitive reasoning. Maximum generation length was set to 3,000 tokens to accommodate longer Chain-of-Thought outputs, and sampling was disabled to ensure reproducibility across runs.

For each case, the model produced 13 independent reasoning traces. Final predictions were obtained using a majority-vote aggregation over the extracted diagnostic answers, with ties resolved by selecting the earliest beam. All inputs were encoded with the gpt-oss chat template using left padding and a 4,096-token context window, and inference was executed using the Unslloth runtime with 4-bit quantized weights and attached LoRA adapters. This protocol allowed the model to balance the range of diagnostic reasoning with reliability, resulting in a stable exact-match performance while preserving a clinically interpretable diagnostic rationale.

Statistical analysis

To account for the stochastic nature of Large Language Model (LLM) generation, we employed a self-consistency framework wherein each model was queried three independent times ($k = 3$) for every case. All performance metrics and statistical comparisons were derived from the consensus prediction of these three runs. For nominal tasks, including the general diagnosis questions and ophthalmology specialty-specific questions, the consensus was determined via majority voting, where a prediction was considered correct only if the correct answer was generated in at least two of the three runs. For ordinal tasks evaluated on a 5-point Likert scale (LLM-as-a-judge for diagnosis and treatment scoring), the consensus was defined as the mean score of the three runs to obtain a stable per-case consensus score.

Model performance for nominal tasks was reported as accuracy, with 95% Confidence Intervals (CIs) calculated using the Wilson Score Interval method to provide robust estimates for binomial proportions. For the clinical judge task, performance was reported as the signed median error across cases between the model's mean consensus score and the ground-truth human expert score, summarized using the interquartile range (IQR). Statistical significance between model performances was determined using pairwise hypothesis tests on paired samples evaluated on the same test cases, with a significance threshold of $P < 0.05$. Differences in accuracy for nominal tasks were assessed using McNemar's Test with continuity correction, while differences in the distribution of errors for ordinal clinical judgment tasks were assessed using the Wilcoxon Signed-Rank Test.

We further evaluated both the internal stability of the models and agreement between models using metrics appropriate to the nominal and ordinal structure of the evaluation tasks. To measure generation consistency across the three inference runs (intra-model stability), we calculated Fleiss' Kappa (κ) for nominal datasets and the Intraclass Correlation Coefficient (ICC, form 3,k) for ordinal datasets. To assess the degree to which different models converged on identical predictions independent of ground truth (inter-model agreement), we calculated standard Cohen's Kappa for nominal tasks. For ordinal LLM-as-a-judge scoring tasks, Linear Weighted Kappa was employed to penalize partial disagreements (e.g., scores of 4 vs. 5) less severely than complete disagreements.

Data Availability

The benchmarking results and model outputs generated in this study are available in the Supplementary Information. The raw input data for the general diagnosis task are available from the Eurorad library (<https://www.eurorad.org/>); a script to retrieve the specific cases used in this study is provided in the code repository. The ophthalmology and clinical judge datasets are publicly available at <https://github.com/bowang-lab/on-device-LLM>. The training dataset with gpt-oss-120b reasoning enhancement used to fine-tune the model is available at <https://huggingface.co/datasets/omareng/eurorad-gpt-oss-training-data>.

Code Availability

The code for model inference, benchmarking, and evaluation is publicly available on GitHub at <https://github.com/bowang-lab/on-device-LLM>. The fine-tuned model weights are available on HuggingFace at <https://huggingface.co/omareng/on-device-LLM-gpt-oss-20b>.

Acknowledgements

This work was supported by the Natural Sciences and Engineering Research Council of Canada (RGPIN-2020-06189 and DGECR-2020-00294) and CIFAR AI Chair programs. This research was enabled, in part, by computing resources provided by the Digital Research Alliance of Canada.

REFERENCES

- [1] D. Van Veen, C. Van Uden, L. Blankemeier, J.-B. Delbrouck, A. Aali, C. Bluethgen, A. Pareek, M. Polacin, E. P. Reis, A. Seehofnerová, N. Rohatgi, P. Hosamani, W. Collins, N. Ahuja, C. P. Langlotz, J. Hom, S. Gatidis, J. Pauly, and A. S. Chaudhari, "Adapted large language models can outperform medical experts in clinical text summarization," *Nature Medicine*, vol. 30, no. 4, p. 1134–1142, 2024.
- [2] X. Liu, H. Liu, G. Yang, Z. Jiang, S. Cui, Z. Zhang, H. Wang, L. Tao, Y. Sun, Z. Song, T. Hong, J. Yang, T. Gao, J. Zhang, X. Li, J. Zhang, Y. Sang, Z. Yang, K. Xue, S. Wu, P. Zhang, J. Yang, C. Song, and G. Wang, "A generalist medical language model for disease diagnosis assistance," *Nature Medicine*, vol. 31, no. 3, pp. 932–942, 2025.
- [3] K. Singhal, S. Azizi, T. Tu, S. S. Mahdavi, J. Wei, H. W. Chung, N. Scales, A. Tanwani, H. Cole-Lewis, S. Pfohl, P. Payne, M. Seneviratne, P. Gamble, C. Kelly, A. Babiker, N. Schärli, A. Chowdhery, P. Mansfield, D. Demner-Fushman, B. Agüera y Arcas, D. Webster, G. S. Corrado, Y. Matias, K. Chou, J. Gottweis, N. Tomasev, Y. Liu, A. Rajkomar, J. Barral, C. Semturs, A. Karthikesalingam, and V. Natarajan, "Large language models encode clinical knowledge," *Nature*, vol. 620, no. 7972, p. 172–180, 2023.
- [4] K. Singhal, T. Tu, J. Gottweis, R. Sayres, E. Wulczyn, M. Amin, L. Hou, K. Clark, S. R. Pfohl, H. Cole-Lewis, D. Neal, Q. M. Rashid, M. Schaeckermann, A. Wang, D. Dash, J. H. Chen, N. H. Shah, S. Lachgar, P. A. Mansfield, S. Prakash, B. Green, E. Dominowska, B. Agüera y Arcas, N. Tomasev, Y. Liu, R. Wong, C. Semturs, S. S. Mahdavi, J. K. Barral, D. R. Webster, G. S. Corrado, Y. Matias, S. Azizi, A. Karthikesalingam, and V. Natarajan, "Toward expert-level medical question answering with large language models," *Nature Medicine*, vol. 31, no. 3, p. 943–950, 2025.
- [5] D. McDuff, M. Schaeckermann, T. Tu, A. Palepu, A. Wang, J. Garrison, K. Singhal, Y. Sharma, S. Azizi, K. Kulkarni, L. Hou, Y. Cheng, Y. Liu, S. S. Mahdavi, S. Prakash, A. Pathak, C. Semturs, S. Patel, D. R. Webster, E. Dominowska, J. Gottweis, J. Barral, K. Chou, G. S. Corrado, Y. Matias, J. Sunshine, A. Karthikesalingam, and V. Natarajan, "Towards accurate differential diagnosis with large language models," *Nature*, vol. 642, no. 8067, p. 451–457, 2025.
- [6] T. Tu, M. Schaeckermann, A. Palepu, K. Saab, J. Freyberg, R. Tanno, A. Wang, B. Li, M. Amin, Y. Cheng, E. Vedadi, N. Tomasev, S. Azizi, K. Singhal, L. Hou, A. Webson, K. Kulkarni, S. S. Mahdavi, C. Semturs, J. Gottweis, J. Barral, K. Chou, G. S. Corrado, Y. Matias, A. Karthikesalingam, and V. Natarajan, "Towards conversational diagnostic artificial intelligence," *Nature*, vol. 642, no. 8067, p. 442–450, Apr. 2025.
- [7] R. Korom, S. Kiptinness, N. Adan, K. Said, C. Ithuli, O. Rotich, B. Kimani, I. King'ori, S. Kamau, E. Atemba *et al.*, "AI-based clinical decision support for primary care: A real-world study," *arXiv preprint arXiv:2507.16947*, 2025.
- [8] D. Guo, D. Yang, H. Zhang, J. Song, P. Wang, Q. Zhu, R. Xu, R. Zhang, S. Ma, X. Bi, X. Zhang, X. Yu, Y. Wu, Z. F. Wu, Z. Gou, Z. Shao, Z. Li, Z. Gao, A. Liu, B. Xue, B. Wang, B. Wu, B. Feng, C. Lu, C. Zhao, C. Deng, C. Ruan, D. Dai, D. Chen, D. Ji, E. Li, F. Lin, F. Dai, F. Luo, G. Hao, G. Chen, G. Li, H. Zhang, H. Xu, H. Ding, H. Gao, H. Qu, H. Li, J. Guo, J. Li, J. Chen, J. Yuan, J. Tu, J. Qiu, J. Li, J. L. Cai, J. Ni, J. Liang, J. Chen, K. Dong, K. Hu, K. You, K. Gao, K. Guan, K. Huang, K. Yu, L. Wang, L. Zhang, L. Zhao, L. Wang, L. Zhang, L. Xu, L. Xia, M. Zhang, M. Zhang, M. Tang, M. Zhou, M. Li, M. Wang, M. Li, N. Tian, P. Huang, P. Zhang, Q. Wang, Q. Chen, Q. Du, R. Ge, R. Zhang, R. Pan, R. Wang, R. J. Chen, R. L. Jin, R. Chen, S. Lu, S. Zhou, S. Chen, S. Ye, S. Wang, S. Yu, S. Zhou, S. Pan, S. S. Li, S. Zhou, S. Wu, T. Yun, T. Pei, T. Sun, T. Wang, W. Zeng, W. Liu, W. Liang, W. Gao, W. Yu, W. Zhang, W. L. Xiao, W. An, X. Liu, X. Wang, X. Chen, X. Nie, X. Cheng, X. Liu, X. Xie, X. Liu, X. Yang, X. Li, X. Su, X. Lin, X. Q. Li, X. Jin, X. Shen, X. Chen, X. Sun, X. Wang, X. Song, X. Zhou, X. Wang, X. Shan, Y. K. Li, Y. Q. Wang, Y. X. Wei, Y. Zhang, Y. Xu, Y. Li, Y. Zhao, Y. Sun, Y. Wang, Y. Yu, Y. Zhang, Y. Shi, Y. Xiong, Y. He, Y. Piao, Y. Wang, Y. Tan, Y. Ma, Y. Liu, Y. Guo, Y. Ou, Y. Wang, Y. Gong, Y. Zou, Y. He, Y. Xiong, Y. Luo, Y. You, Y. Liu, Y. Zhou, Y. X. Zhu, Y. Huang, Y. Li, Y. Zheng, Y. Zhu, Y. Ma, Y. Tang, Y. Zha, Y. Yan, Z. Z. Ren, Z. Ren, Z. Sha, Z. Fu, Z. Xu, Z. Xie, Z. Zhang, Z. Hao, Z. Ma, Z. Yan, Z. Wu, Z. Gu, Z. Zhu, Z. Liu, Z. Li, Z. Xie, Z. Song, Z. Pan, Z. Huang, Z. Xu, Z. Zhang, and Z. Zhang, "DeepSeek-R1 incentivizes reasoning in LLMs through reinforcement learning," *Nature*, vol. 645, no. 8081, p. 633–638, 2025.
- [9] M. Tordjman, Z. Liu, M. Yuce, F. Fauveau, Y. Mei, J. Hadjadj, I. Bolger, H. Almansour, C. Horst, A. S. Parihar, A. Geahchan, A. Meribout, N. Yatim, N. Ng, P. Robson, A. Zhou, S. Lewis, M. Huang, T. Deyer, B. Taouli, H.-C. Lee, Z. A. Fayad, and X. Mei, "Comparative benchmarking of the deepseek large language model on medical tasks and clinical reasoning," *Nature Medicine*, vol. 31, no. 8, p. 2550–2555, 2025.
- [10] S. Sandmann, S. Hegselmann, M. Fujarski, L. Bickmann, B. Wild, R. Eils, and J. Varghese, "Benchmark evaluation of deepseek large language models in clinical decision-making," *Nature Medicine*, vol. 31, no. 8, p. 2546–2549, 2025.

[11] OpenAI, S. Agarwal, L. Ahmad, J. Ai, S. Altman, A. Applebaum, E. Arbus, R. K. Arora, Y. Bai, B. Baker, H. Bao, B. Barak, A. Bennett, T. Bertao, N. Brett, E. Brevdo, G. Brockman, S. Bubeck, C. Chang, K. Chen, M. Chen, E. Cheung, A. Clark, D. Cook, M. Dukhan, C. Dvorak, K. Fives, V. Fomenko, T. Garipov, K. Georgiev, M. Glaese, T. Gogineni, A. Goucher, L. Gross, K. G. Guzman, J. Hallman, J. Hehir, J. Heidecke, A. Helyar, H. Hu, R. Huet, J. Huh, S. Jain, Z. Johnson, C. Koch, I. Kofman, D. Kundel, J. Kwon, V. Kyrylov, E. Y. Le, G. Leclerc, J. P. Lennon, S. Lessans, M. Lezcano-Casado, Y. Li, Z. Li, J. Lin, J. Liss, L. X. Liu, J. Liu, K. Lu, C. Lu, Z. Martinovic, L. McCallum, J. McGrath, S. McKinney, A. McLaughlin, S. Mei, S. Mostovoy, T. Mu, G. Myles, A. Neitz, A. Nichol, J. Pachocki, A. Paino, D. Palmie, A. Pantuliano, G. Parascandolo, J. Park, L. Pathak, C. Paz, L. Peran, D. Pimenov, M. Pokrass, E. Proehl, H. Qiu, G. Raila, F. Raso, H. Ren, K. Richardson, D. Robinson, B. Rotsted, H. Salman, S. Sanjeev, M. Schwarzer, D. Sculley, H. Sikchi, K. Simon, K. Singhal, Y. Song, D. Stuckey, Z. Sun, P. Tillet, S. Toizer, F. Tsimpourlas, N. Vyas, E. Wallace, X. Wang, M. Wang, O. Watkins, K. Weil, A. Wendling, K. Whinnery, C. Whitney, H. Wong, L. Yang, Y. Yang, M. Yasunaga, K. Ying, W. Zaremba, W. Zhan, C. Zhang, B. Zhang, E. Zhang, and S. Zhao, "gpt-oss-120b & gpt-oss-20b model card," *arXiv preprint arXiv:2508.10925*, 2025.

[12] P. Xu, Y. Wu, K. Jin, X. Chen, M. He, and D. Shi, "DeepSeek-R1 outperforms Gemini 2.0 Pro, OpenAI o1, and o3-mini in bilingual complex ophthalmology reasoning," *Advances in Ophthalmology Practice and Research*, vol. 5, no. 3, pp. 189–195, 2025.

Supplementary

Prompt

Prompt 1. Prompt for General Radiology Diagnosis

You are a careful radiology diagnosis selector. Given a clinical case description and a finite list of candidate diagnoses, choose the single most likely final diagnosis FROM THE LIST.

Response rules:

- 1) Output EXACTLY one option, copied VERBATIM from the list.
- 2) Output ONLY the diagnosis text. No explanation. No punctuation. No quotes.

Prompt

Prompt 2. Prompts for Ophthalmology QA

You are a careful ophthalmology question-answering assistant. You will be given a multiple-choice case with options labeled A-Z. Some questions have a single correct answer, while others have multiple correct answers. Select ALL correct answers. If only one answer is correct, return just that single letter. Respond with ONLY the capital letters (A-Z), concatenated together with no spaces or punctuation (e.g., 'ABE' for multiple answers, or 'D' if only one). Do not explain.

Case: *[Case Data Inserted Here]*

Task: Choose the correct answer(s).

Return: One or more letters from A to Z, concatenated with no spaces (e.g., ABE or D).

Prompt

Prompt 3. Prompt for LLM-as-a-Clinical-Judge on Diagnosis Tasks

You are asked to evaluate the quality of a model's diagnostic output using the following rubric:

Scoring Rubric (Likert scale 1–5):

1. Most relevant diagnoses not mentioned.
2. Many relevant diagnoses missing or incorrectly identified.
3. Some relevant diagnoses mentioned, but important omissions or inaccuracies present.
4. Most relevant diagnoses correctly identified, with only minor omissions.
5. All relevant diagnoses correctly identified.

Instruction:

Given the following task description, the true disease, and the model output, assign a single integer score from 1 to 5 according to the rubric. Half-point scores (e.g., 1.5, 2.5, 3.5, 4.5) are allowed if the quality falls between two rubric levels. Output **only the score**, with no explanation or justification.

Inputs:

[Case Data Inserted Here]

Prompt

Prompt 4. Prompt for LLM-as-a-Clinical-Judge on Treatment Tasks

You are asked to evaluate the quality of a model's treatment suggestion output using the following rubric:

Scoring Rubric (Likert scale 1–5):

1. All or most suggested options redundant or unjustified.
2. Some suggested options redundant or unjustified.
3. Most suggested options appropriate, but minor redundancy or weak justification present.
4. Few suggested options redundant or unjustified.
5. No suggested options redundant or unjustified.

Instruction:

Given the following task description, the true disease, and the model output, assign a score from 1 to 5 according to the rubric. Half-point scores (e.g., 1.5, 2.5, 3.5, 4.5) are allowed if the quality falls between two rubric levels. Output **only the score**, with no explanation or justification.

Inputs:

[Case Data Inserted Here]

Prompt

Prompt 5. Prompt for Reasoning Data Generation, Fine-tuning gpt-oss-20b, and Inference (Same prompt for all)

You are an expert radiologist demonstrating step-by-step diagnostic reasoning.

Case presentation:

[Case Data Inserted Here]

Differential diagnoses to consider:

[Answer Options]

Generate systematic Chain-of-Thought reasoning that shows how clinicians think through cases:

1. **Connect symptoms to findings:** Link clinical presentation with imaging observations
2. **Map to differentials:** Show how findings support or contradict each differential diagnosis
3. **Systematic elimination:** Explicitly rule out less likely options with reasoning
4. **Converge to answer:** Demonstrate the logical path to the correct diagnosis

TABLE 1

LLM-as-a-Generalist Task: Comparative diagnostic accuracy across radiological anatomical subgroups. Performance is evaluated using self-consistency majority voting accuracy (%, 95% CI). While the proprietary GPT-5 sets the highest overall average performance (88.9% average), the on-device gpt-oss-120b (L) model achieves an average accuracy of 82.3%, effectively matching the open-source frontier DeepSeek-R1 (82.3%) and approaching the efficient proprietary baseline o4-mini (85.2%).

Category	GPT-5	o4-mini	DeepSeek-R1	gpt-oss-20b (L)	gpt-oss-20b (M)	gpt-oss-20b (H)	gpt-oss-120b (L)	gpt-oss-120b (M)	gpt-oss-120b (H)
Musculoskeletal system	87.2 (74.8–94.0)	85.1 (72.3–92.6)	87.2 (74.8–94.0)	80.9 (67.5–89.6)	85.1 (72.3–92.6)	87.2 (74.8–94.0)	89.4 (77.4–95.4)	83.0 (69.9–91.1)	85.1 (72.3–92.6)
Cardiovascular	83.3 (43.6–97.0)	83.3 (43.6–97.0)	66.7 (30.0–90.3)	50.0 (18.8–81.2)	50.0 (18.8–81.2)	50.0 (18.8–81.2)	66.7 (30.0–90.3)	66.7 (30.0–90.3)	66.7 (30.0–90.3)
Abdominal imaging	94.4 (81.9–98.5)	83.3 (43.6–97.0)	75.0 (58.9–86.2)	63.9 (47.6–77.5)	66.7 (50.3–79.8)	80.6 (65.0–90.2)	86.1 (71.3–93.9)	83.3 (68.1–92.1)	83.3 (68.1–92.1)
Uroradiology & genital male imaging	100.0 (72.2–100.0)	86.1 (71.3–93.9)	100.0 (72.2–100.0)	80.0 (49.0–94.3)	90.0 (59.6–98.2)	100.0 (72.2–100.0)	90.0 (59.6–98.2)	100.0 (72.2–100.0)	90.0 (59.6–98.2)
Neuroradiology	85.4 (71.6–93.1)	82.9 (68.7–91.5)	85.4 (71.6–93.1)	82.9 (68.7–91.5)	82.9 (68.7–91.5)	85.4 (71.6–93.1)	82.9 (68.7–91.5)	80.5 (66.0–89.8)	85.4 (71.6–93.1)
Paediatric radiology	83.3 (66.4–92.7)	76.7 (59.1–88.2)	73.3 (55.6–85.8)	73.3 (55.6–85.8)	76.7 (59.1–88.2)	70.0 (52.1–83.3)	76.7 (59.1–88.2)	73.3 (55.6–85.8)	80.0 (62.7–90.5)
Head & neck imaging	100.0 (77.2–100.0)	100.0 (77.2–100.0)	84.6 (57.8–95.7)	84.6 (57.8–95.7)	84.6 (57.8–95.7)	92.3 (66.7–98.6)	100.0 (77.2–100.0)	76.9 (49.7–91.8)	92.3 (66.7–98.6)
Breast imaging	100.0 (56.6–100.0)	80.0 (37.6–96.4)	80.0 (37.6–96.4)	40.0 (11.8–76.9)	40.0 (11.8–76.9)	40.0 (11.8–76.9)	60.0 (23.1–88.2)	60.0 (23.1–88.2)	60.0 (23.1–88.2)
Chest imaging	90.9 (62.3–98.4)	81.8 (52.3–94.9)	81.8 (52.3–94.9)	72.7 (43.4–90.3)	81.8 (52.3–94.9)	81.8 (52.3–94.9)	81.8 (52.3–94.9)	81.8 (52.3–94.9)	81.8 (52.3–94.9)
Others	75.0 (40.9–92.9)	75.0 (40.9–92.9)	75.0 (40.9–92.9)	62.5 (30.6–86.3)	62.5 (30.6–86.3)	62.5 (30.6–86.3)	75.0 (40.9–92.9)	75.0 (40.9–92.9)	62.5 (30.6–86.3)
Average	88.9 (83.9–92.5)	84.1 (78.5–88.4)	81.6 (75.8–86.3)	74.4 (68.0–79.9)	77.3 (71.1–82.5)	80.7 (74.8–85.5)	84.1 (78.5–88.4)	80.2 (74.2–85.1)	82.6 (76.9–87.2)

TABLE 2

LLM-as-a-Specialist Task: Comparative accuracy on ophthalmology diagnosis and management tasks. Performance is evaluated across distinct clinical subspecialties and question types (Diagnosis vs. Management). Scores are presented as accuracy percentages (95% confidence intervals). The open-source DeepSeek-R1 achieves the highest overall accuracy, while the on-device gpt-oss-120b (M) surpasses the proprietary baselines GPT-5 and o4-mini.

Type	Topic	GPT-5	o4-mini	DeepSeek-R1	gpt-oss-20b (L)	gpt-oss-20b (M)	gpt-oss-20b (H)	gpt-oss-120b (L)	gpt-oss-120b (M)	gpt-oss-120b (H)
Diagnosis	Glaucoma	100.0 (64.6–100.0)	85.7 (48.7–97.4)	100.0 (64.6–100.0)	71.4 (35.9–91.8)	85.7 (48.7–97.4)	85.7 (48.7–97.4)	85.7 (48.7–97.4)	85.7 (48.7–97.4)	85.7 (48.7–97.4)
	External Eye/Orbital Diseases	80.0 (49.0–94.3)	80.0 (49.0–94.3)	90.0 (59.6–98.2)	70.0 (39.7–89.2)	70.0 (39.7–89.2)	80.0 (49.0–94.3)	70.0 (39.7–89.2)	80.0 (49.0–94.3)	80.0 (49.0–94.3)
	Retinal Diseases	100.0 (43.8–100.0)	100.0 (43.8–100.0)	100.0 (43.8–100.0)	66.7 (20.8–93.9)	66.7 (20.8–93.9)	66.7 (20.8–93.9)	100.0 (43.8–100.0)	66.7 (20.8–93.9)	66.7 (20.8–93.9)
	Anterior Segment Diseases	62.5 (30.6–86.3)	75.0 (40.9–92.9)	75.0 (40.9–92.9)	62.5 (30.6–86.3)	62.5 (30.6–86.3)	62.5 (30.6–86.3)	75.0 (40.9–92.9)	75.0 (40.9–92.9)	75.0 (40.9–92.9)
	Ocular Trauma	100.0 (61.0–100.0)	83.3 (43.6–97.0)	100.0 (61.0–100.0)	83.3 (43.6–97.0)	66.7 (30.0–90.3)	83.3 (43.6–97.0)	83.3 (43.6–97.0)	100.0 (61.0–100.0)	83.3 (43.6–97.0)
	Refractive Disorders/Strabismus	100.0 (56.6–100.0)	100.0 (56.6–100.0)	100.0 (56.6–100.0)	100.0 (56.6–100.0)	100.0 (56.6–100.0)	100.0 (56.6–100.0)	100.0 (56.6–100.0)	100.0 (56.6–100.0)	100.0 (56.6–100.0)
<i>Average</i>		87.2 (73.3–94.4)	84.6 (70.3–92.8)	92.3 (79.7–97.3)	74.4 (58.9–85.4)	74.4 (58.9–85.4)	79.5 (64.5–89.2)	82.1 (67.3–91.0)	84.6 (70.3–92.8)	82.1 (67.3–91.0)
Management	Glaucoma	78.6 (52.4–92.4)	64.3 (38.8–83.7)	71.4 (45.4–88.3)	50.0 (26.8–73.2)	64.3 (38.8–83.7)	50.0 (26.8–73.2)	71.4 (45.4–88.3)	78.6 (52.4–92.4)	64.3 (38.8–83.7)
	External Eye/Orbital Diseases	78.6 (52.4–92.4)	64.3 (38.8–83.7)	78.6 (52.4–92.4)	57.1 (32.6–78.6)	71.4 (45.4–88.3)	64.3 (38.8–83.7)	71.4 (45.4–88.3)	71.4 (45.4–88.3)	71.4 (45.4–88.3)
	Retinal Diseases	37.5 (13.7–69.4)	37.5 (13.7–69.4)	37.5 (13.7–69.4)	12.5 (2.2–47.1)	25.0 (7.1–59.1)	37.5 (13.7–69.4)	50.0 (21.5–78.5)	37.5 (13.7–69.4)	37.5 (13.7–69.4)
	Anterior Segment Diseases	70.6 (46.9–86.7)	64.7 (41.3–82.7)	70.6 (46.9–86.7)	76.5 (52.7–90.4)	64.7 (41.3–82.7)	76.5 (52.7–90.4)	70.6 (46.9–86.7)	76.5 (52.7–90.4)	70.6 (46.9–86.7)
	Ocular Trauma	57.7 (38.9–74.5)	69.2 (50.0–83.5)	76.9 (57.9–89.0)	42.3 (25.5–61.1)	57.7 (38.9–74.5)	50.0 (32.1–67.9)	65.4 (46.2–80.6)	76.9 (57.9–89.0)	57.7 (38.9–74.5)
	Refractive Disorders/Strabismus	83.3 (55.2–95.3)	83.3 (55.2–95.3)	91.7 (64.6–98.5)	66.7 (39.1–86.2)	58.3 (32.0–80.7)	83.3 (55.2–95.3)	83.3 (55.2–95.3)	91.7 (64.6–98.5)	83.3 (55.2–95.3)
<i>Average</i>		68.1 (58.0–76.8)	65.9 (55.7–74.8)	73.6 (63.7–81.6)	52.7 (42.6–62.7)	59.3 (49.1–68.9)	60.4 (50.2–69.9)	69.2 (59.1–77.8)	74.7 (64.9–82.5)	64.8 (54.6–73.9)
Overall		73.8 (65.7–80.6)	71.5 (63.3–78.6)	79.2 (71.5–85.3)	59.2 (50.6–67.3)	63.8 (55.3–71.6)	66.2 (57.7–73.7)	73.1 (64.9–80.0)	77.7 (69.8–84.0)	70.0 (61.6–77.2)

TABLE 3

LLM-as-a-Clinical-Judge Task: Comparative performance on treatment and diagnosis across five specialties. Scores are presented as the median error (25%-75% interquartile range, IQR) relative to human expert scores. A value of 0 indicates perfect alignment, while negative values indicate the model underestimated the clinical score.

Type	Topic	GPT-5	o4-mini	DeepSeek-R1	gpt-oss-20b (L)	gpt-oss-20b (M)	gpt-oss-20b (H)	gpt-oss-120b (L)	gpt-oss-120b (M)	gpt-oss-120b (H)
Treatment	Gynecology	-0.04 (-0.75–0.50)	0.00 (0.00–0.50)	0.38 (0.00–0.67)	0.17 (-0.02–0.52)	0.17 (-0.33–0.50)	0.17 (-0.10–0.50)	0.00 (-0.35–0.50)	0.17 (-0.33–0.50)	0.00 (-0.25–0.50)
	Internal Medicine	0.00 (-0.25–0.50)	0.08 (0.00–0.50)	0.17 (0.00–0.50)	0.00 (-0.33–0.50)	0.00 (-0.08–0.50)	0.00 (-0.17–0.50)	0.00 (-0.08–0.50)	0.00 (-0.08–0.50)	0.00 (-0.17–0.50)
	Neurology	0.50 (0.00–0.83)	0.50 (0.00–1.00)	0.21 (0.00–0.83)	0.00 (-0.17–0.67)	0.17 (-0.17–0.50)	0.00 (-0.33–0.50)	0.17 (-0.17–0.50)	0.17 (-0.17–0.67)	0.17 (0.00–0.67)
	Pediatrics	0.00 (-0.33–0.50)	0.00 (0.00–0.50)	0.17 (0.00–0.50)	0.00 (-0.33–0.50)	0.00 (-0.33–0.50)	0.00 (-0.33–0.50)	0.17 (-0.17–0.50)	0.00 (-0.19–0.50)	0.04 (-0.17–0.50)
	Surgery	0.17 (-0.17–0.83)	0.42 (0.00–1.00)	0.50 (0.00–1.00)	0.25 (-0.08–0.83)	0.33 (0.00–1.00)	0.50 (-0.08–1.00)	0.33 (0.00–1.00)	0.50 (0.00–1.00)	0.50 (0.00–1.00)
	Overall	0.00 (-0.33–0.50)	0.25 (0.00–0.63)	0.29 (0.00–0.67)	0.08 (-0.17–0.50)	0.17 (-0.17–0.50)	0.17 (-0.29–0.50)	0.17 (-0.17–0.50)	0.17 (-0.17–0.58)	0.17 (-0.17–0.50)
Diagnosis	Gynecology	-0.33 (-0.83–0.00)	-0.50 (-1.33–0.00)	-0.17 (-0.50–0.00)	-0.17 (-0.50–0.00)	-0.17 (-0.67–0.00)	-0.33 (-0.67–0.00)	0.00 (-0.33–0.00)	0.00 (-0.33–0.00)	0.00 (-0.33–0.08)
	Internal Medicine	-0.33 (-1.00–0.00)	-1.25 (-2.00–0.33)	-0.33 (-0.75–0.00)	-0.33 (-1.00–0.00)	-0.33 (-0.69–0.00)	-0.33 (-0.94–0.00)	0.00 (-0.50–0.25)	0.00 (-0.50–0.33)	0.00 (-0.54–0.33)
	Neurology	-0.71 (-1.50–0.17)	-1.00 (-1.92–0.33)	-0.33 (-0.67–0.00)	-0.33 (-1.02–0.00)	-0.33 (-1.00–0.00)	-0.17 (-1.17–0.00)	-0.17 (-1.50–0.17)	-0.17 (-1.54–0.17)	-0.17 (-1.67–0.17)
	Pediatrics	-0.50 (-1.08–0.00)	-1.00 (-2.00–0.33)	-0.33 (-0.67–0.00)	-0.33 (-0.83–0.00)	-0.33 (-0.79–0.00)	-0.33 (-0.67–0.00)	0.00 (-0.50–0.23)	0.00 (-0.50–0.17)	0.00 (-0.33–0.25)
	Surgery	-0.33 (-0.83–0.00)	-0.67 (-1.69–0.00)	-0.17 (-0.50–0.17)	0.00 (-0.50–0.33)	0.00 (-0.58–0.33)	0.00 (-0.58–0.27)	0.00 (-0.50–0.37)	0.00 (-0.33–0.50)	0.00 (-0.35–0.50)
	Overall	-0.50 (-1.00–0.00)	-1.00 (-1.83–0.17)	-0.33 (-0.67–0.00)	-0.33 (-0.67–0.00)	-0.25 (-0.67–0.00)	-0.25 (-0.67–0.00)	0.00 (-0.50–0.25)	0.00 (-0.50–0.25)	0.00 (-0.50–0.25)

TABLE 4

LLM-as-a-Clinical-Judge Task: Impact of disease prevalence on clinical judgment accuracy. Model alignment with human expert scoring is stratified by disease frequency (Rare, Less Frequent, Frequent). Scores are presented as the median error (25%-75% interquartile range, IQR) relative to human expert scores.

Type	Frequency	GPT-5	o4-mini	DeepSeek-R1	gpt-oss-20b (L)	gpt-oss-20b (M)	gpt-oss-20b (H)	gpt-oss-120b (L)	gpt-oss-120b (M)	gpt-oss-120b (H)
Treatment	Rare	0.00 (0.00–0.50)	0.25 (0.00–0.50)	0.25 (0.00–0.67)	0.00 (-0.17–0.50)	0.08 (-0.17–0.50)	0.00 (-0.33–0.50)	0.17 (0.00–0.50)	0.00 (-0.17–0.50)	0.00 (-0.17–0.50)
	Less Frequent	0.00 (-0.33–0.50)	0.29 (0.00–0.75)	0.42 (0.00–0.50)	0.17 (-0.17–0.50)	0.17 (-0.17–0.50)	0.17 (-0.31–0.50)	0.17 (0.00–0.50)	0.25 (0.00–0.63)	0.25 (0.00–0.65)
	Frequent	0.00 (-0.50–0.50)	0.17 (0.00–0.50)	0.17 (0.00–0.71)	0.00 (-0.27–0.50)	0.00 (-0.17–0.67)	0.17 (-0.17–0.50)	0.17 (-0.17–0.50)	0.17 (-0.17–0.58)	0.17 (-0.17–0.50)
<i>Overall</i>		0.00 (-0.33–0.50)	0.25 (0.00–0.63)	0.29 (0.00–0.67)	0.08 (-0.17–0.50)	0.17 (-0.17–0.50)	0.17 (-0.29–0.50)	0.17 (-0.17–0.50)	0.17 (-0.17–0.58)	0.17 (-0.17–0.50)
Diagnosis	Rare	-0.67 (-1.25–0.00)	-1.25 (-2.00–0.50)	-0.33 (-0.92–0.08)	-0.33 (-1.17–0.00)	-0.33 (-1.08–0.08)	-0.33 (-1.17–0.13)	0.00 (-1.29–0.42)	0.00 (-1.38–0.33)	0.00 (-1.25–0.33)
	Less Frequent	-0.33 (-1.08–0.00)	-1.00 (-1.83–0.33)	-0.29 (-0.67–0.00)	-0.33 (-0.83–0.00)	-0.33 (-0.67–0.00)	-0.33 (-0.67–0.00)	0.00 (-0.67–0.17)	0.00 (-0.67–0.23)	0.00 (-0.67–0.25)
	Frequent	-0.33 (-0.83–0.00)	-0.63 (-1.50–0.00)	-0.25 (-0.50–0.00)	0.00 (-0.33–0.00)	0.00 (-0.50–0.00)	-0.04 (-0.50–0.00)	0.00 (-0.33–0.17)	0.00 (-0.23–0.25)	0.00 (-0.33–0.25)
<i>Overall</i>		-0.50 (-1.00–0.00)	-1.00 (-1.83–0.17)	-0.33 (-0.67–0.00)	-0.33 (-0.67–0.00)	-0.25 (-0.67–0.00)	-0.25 (-0.67–0.00)	0.00 (-0.50–0.25)	0.00 (-0.50–0.25)	0.00 (-0.50–0.25)

TABLE 5

LLM-as-a-Generalist Task: Comparative diagnostic accuracy of fine-tuned gpt-oss-20b model. Diagnostic accuracy (95% confidence interval, CI) is compared between the base gpt-oss-20b model and its fine-tuned counterpart, both evaluated at medium (M) reasoning effort.

Category	GPT-5	o4-mini	DeepSeek-R1	gpt-oss-20b (M)	Fine-tuned gpt-oss-20b (M)
Musculoskeletal system	87.2 (74.8–94.0)	85.1 (72.3–92.6)	87.2 (74.8–94.0)	85.1 (72.3–92.6)	91.5 (80.1–96.6)
Cardiovascular	83.3 (43.6–97.0)	83.3 (43.6–97.0)	66.7 (30.0–90.3)	50.0 (18.8–81.2)	83.3 (43.6–97.0)
Abdominal imaging	94.4 (81.9–98.5)	83.3 (43.6–97.0)	75.0 (58.9–86.2)	66.7 (50.3–79.8)	86.1 (71.3–93.9)
Uroradiology & genital male	100.0 (72.2–100.0)	86.1 (71.3–93.9)	100.0 (72.2–100.0)	90.0 (59.6–98.2)	100.0 (72.2–100.0)
Neuroradiology	85.4 (71.6–93.1)	82.9 (68.7–91.5)	85.4 (71.6–93.1)	82.9 (68.7–91.5)	87.8 (74.5–94.7)
Paediatric radiology	83.3 (66.4–92.7)	76.7 (59.1–88.2)	73.3 (55.6–85.8)	76.7 (59.1–88.2)	73.3 (55.6–85.8)
Head & neck imaging	100.0 (77.2–100.0)	100.0 (77.2–100.0)	84.6 (57.8–95.7)	84.6 (57.8–95.7)	92.3 (66.7–98.6)
Breast imaging	100.0 (56.6–100.0)	80.0 (37.6–96.4)	80.0 (37.6–96.4)	40.0 (11.8–76.9)	80.0 (37.6–96.4)
Chest imaging	90.9 (62.3–98.4)	81.8 (52.3–94.9)	81.8 (52.3–94.9)	81.8 (52.3–94.9)	90.9 (62.3–98.4)
Others	75.0 (40.9–92.9)	75.0 (40.9–92.9)	75.0 (40.9–92.9)	62.5 (30.6–86.3)	75.0 (40.9–92.9)
Average	88.9 (83.9–92.5)	84.1 (78.5–88.4)	81.6 (75.8–86.3)	77.3 (71.7–82.5)	86.5 (81.1–90.5)

Algorithm 1 Inference protocol for robust diagnostic reasoning. The algorithm employs diverse group beam search to generate multiple independent reasoning paths (B beams, G groups), followed by majority-vote aggregation to mitigate hallucination and select the most consensus-driven diagnosis.

Require:

- 1: \mathcal{C} : Patient Case (History and Imaging Findings)
- 2: \mathcal{L} : List of Differential Diagnoses $\{l_1, l_2, \dots, l_n\}$
- 3: \mathcal{M} : Fine-tuned On-device Model
- 4: Parameters: Number of beams B , Number of groups G , Diversity penalty λ

Ensure:

- 5: \hat{y} : Final Selected Diagnosis
- 6: R : Generated Reasoning Trace associated with \hat{y}

7: **Prompt Construction**

- 8: $P \leftarrow \text{FORMATPROMPT}(\mathcal{C}, \mathcal{L})$ ▷ Inject case and constraints into template
- 9: $T_{in} \leftarrow \text{TOKENIZE}(P)$

10: **Diverse Generation (Exploration)**

- 11: Generate B distinct reasoning paths using Group Beam Search
- 12: $\mathcal{S} \leftarrow \text{GENERATE}(T_{in}, \mathcal{M}, \text{beams} = B, \text{groups} = G, \text{penalty} = \lambda)$ ▷ Return sequences $\{s_1, s_2, \dots, s_B\}$ sorted by beam index
- 13:

14: **Answer Extraction and Normalization**

- 15: $\mathcal{D}_{raw} \leftarrow \emptyset$ ▷ List to store extracted answers
- 16: **for** $i \leftarrow 1$ to B **do**
- 17: $r_i, d_i \leftarrow \text{PARSEOUTPUT}(s_i)$ ▷ Split reasoning (r) and diagnosis (d) via delimiter
- 18: $d_i^{norm} \leftarrow \text{NORMALIZETEXT}(d_i)$ ▷ Lowercase, strip punctuation/whitespace
- 19: $\mathcal{D}_{raw} \leftarrow \mathcal{D}_{raw} \cup \{d_i^{norm}\}$
- 20: **end for**

21: **Majority Vote Aggregation**

- 22: $V \leftarrow \text{COUNTFREQUENCIES}(\mathcal{D}_{raw})$ ▷ Map unique diagnoses to vote counts
- 23: $v_{max} \leftarrow \max(V)$
- 24: $\mathcal{T} \leftarrow \{d \mid V[d] = v_{max}\}$ ▷ Set of diagnoses with the highest vote count

25: **Tie-Breaking and Final Selection**

- 26: **if** $|\mathcal{T}| = 1$ **then**
- 27: $\hat{y} \leftarrow$ element in \mathcal{T}
- 28: **else**
- 29: ▷ Tie-breaker: Select the diagnosis appearing in the earliest beam index
- 30: $\hat{y} \leftarrow$ first $d_i^{norm} \in \mathcal{D}_{raw}$ such that $d_i^{norm} \in \mathcal{T}$
- 31: **end if**
- 32: $idx \leftarrow$ index of first occurrence of \hat{y} in \mathcal{D}_{raw}
- 33: **return** \hat{y}, s_{idx}

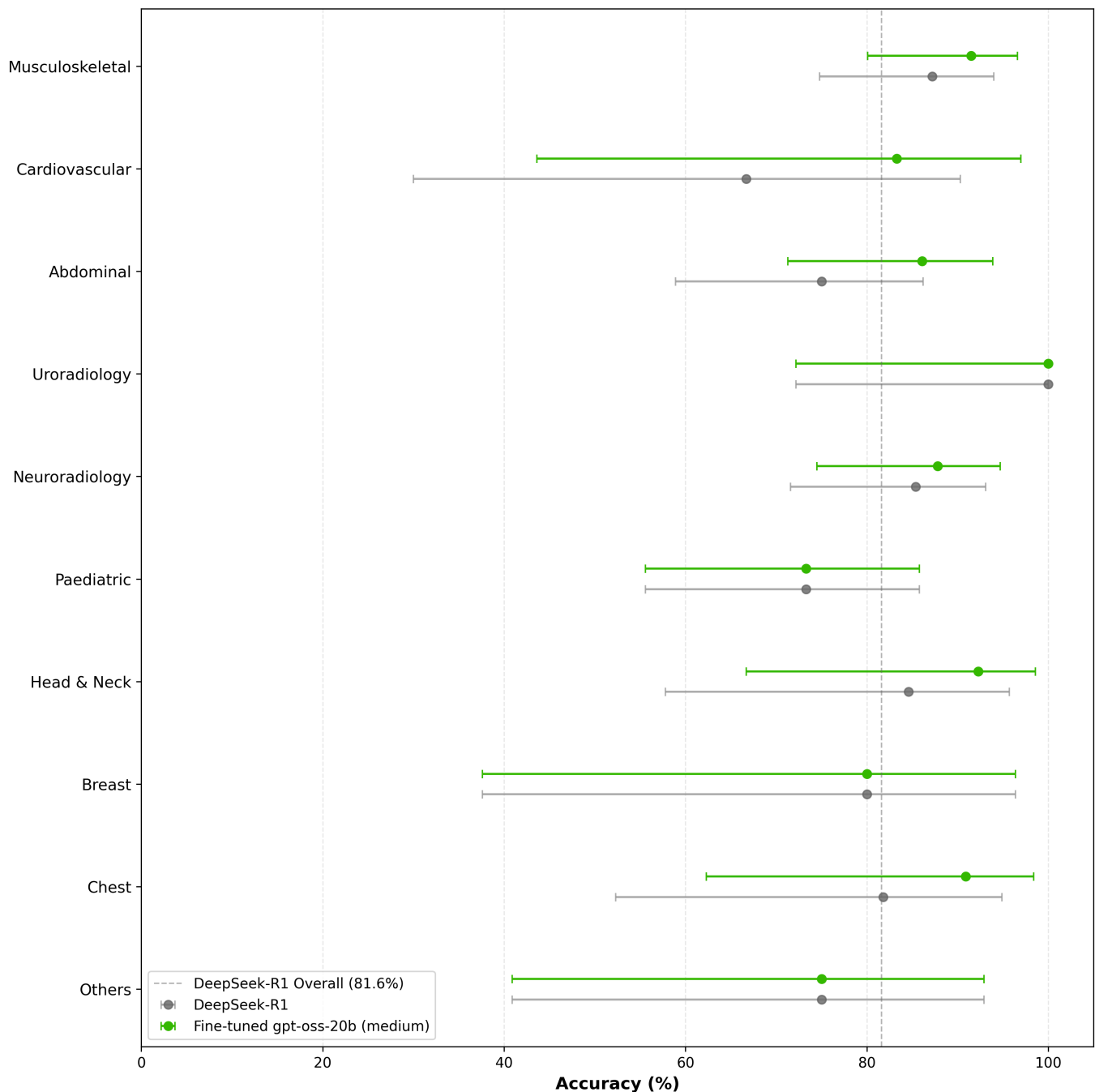


Fig. 1. **Parameter efficiency: Fine-tuned gpt-oss-20b model outperforms the 671B DeepSeek-R1.** Comparative diagnostic accuracy of the fine-tuned gpt-oss-20b model (green) versus the open-source frontier DeepSeek-R1 (gray). Despite being significantly smaller, the fine-tuned on-device model achieves a higher overall micro-average accuracy (86.5% vs 81.6%) and demonstrates superior performance in 7 out of 10 anatomical subgroups. Error bars represent 95% Wilson score intervals.

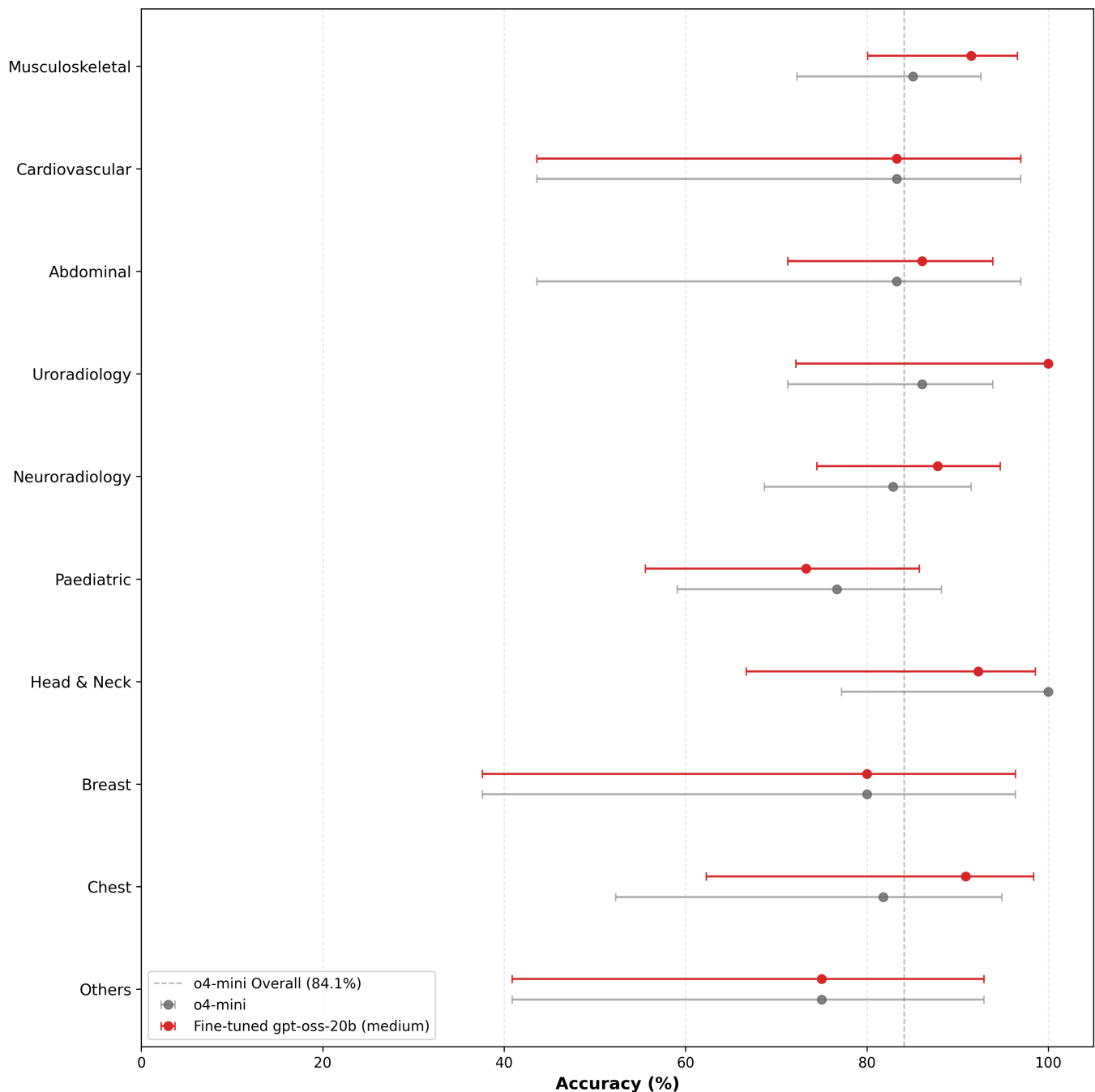


Fig. 2. **On-device versus cloud-based efficiency: Fine-tuned model surpasses o4-mini.** Performance comparison between the fine-tuned gpt-oss-20b (red) and OpenAI's efficient proprietary model, o4-mini (gray). The on-device model demonstrates robust generalization, exceeding the cloud-based baseline in overall accuracy (86.5% vs 84.1%) and achieving competitive results across diverse radiological specialties. Vertical dashed lines indicate the overall micro-average accuracy for each model.

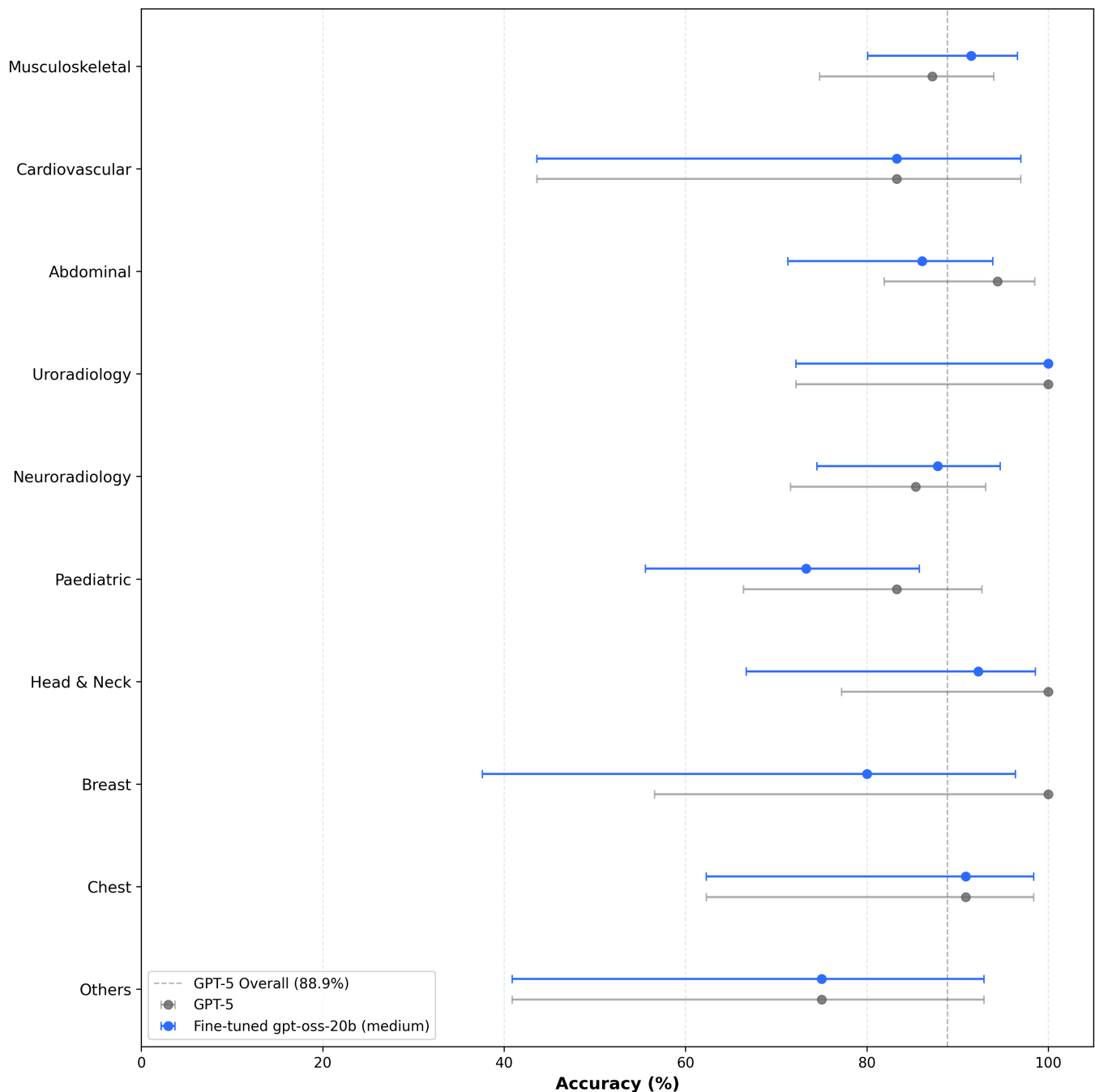


Fig. 3. **Approaching the frontier: On-device model demonstrates competitive performance with GPT-5.** The forest plot illustrates the diagnostic accuracy of the fine-tuned gpt-oss-20b (blue) relative to the state-of-the-art GPT-5 (gray). While GPT-5 maintains a slight lead in overall accuracy (88.9% vs 86.5%), the confidence intervals overlap significantly across the majority of subgroups (e.g., Musculoskeletal, Abdominal, Neuroradiology), indicating statistical parity in these domains.



Fig. 4. **Heatmap of diagnostic accuracy across anatomical subgroups and model architectures.** Color intensity represents accuracy (Green=High, Red=Low). Base on-device models (middle columns) exhibit significant performance degradation in specialized domains such as Cardiovascular and Breast imaging. Fine-tuning the 20b model (far right column) effectively mitigates these domain-specific weaknesses, restoring performance levels comparable to the 120b parameter models and proprietary baselines.

CASE STUDIES

The following case studies illustrate the chain-of-thought reasoning capabilities of gptoss 20b fine-tuned on the Eurorad radiology dataset. Each case demonstrates the model's systematic approach to differential diagnosis: (1) identifying core clinical-radiologic patterns, (2) mapping each differential to observed features, (3) systematically eliminating unlikely diagnoses, and (4) converging on a final answer with supporting rationale.

Case Study

Case Study 1: Von Hippel-Lindau Syndrome

Case Presentation

Clinical History: A 41-year-old male presents with a history of microscopic haematuria, a palpable right flank mass, and recurrent headaches. A CT scan was performed, followed by a brain MRI to rule out tumoural pathology. The patient had no significant medical history.

Imaging Findings: In the abdominal CT scan, multiple bilateral renal cystic lesions with septum formation were observed. The right kidney had multiple, irregular, heterogeneous lesions with significant enhancement post-contrast, and hypodense central areas related to necrosis, the biggest located in the superior pole. Similar characteristics were noted in the left kidney lesions. Also, multiple simple pancreatic cysts and splenic vein dilation were observed, along with pancreaticosplenic collaterals. There is a lesion in the splenic hilum that enhances and follows contrast in different phases, suggestive of a splenic hamartoma. The brain MRI revealed multiple heterogeneous lesions with a cystic and a solid component in the posterior fossa, showing avid and homogeneous enhancement of the solid portion, and causing vasogenic oedema and mass effect on the pons.

Differential diagnoses to consider: Von Hippel-Lindau syndrome (VHL), Sporadic haemangioblastomas, Multiple endocrine neoplasia type 1 (MEN-1), Tuberous sclerosis complex (TSC), Polycystic kidney disease (PKD), Hereditary leiomyomatosis and renal cell cancer (HLRCC)

Ground Truth: Von Hippel-Lindau syndrome (VHL)

Base Model Response (Before Fine-Tuning)

We need to consider the constellation: renal cystic lesions with septations, bilateral; pancreatic cysts; splenic hamartoma; brain hemangioblastomas. Also hematuria, flank mass. *[Issue: Lists features but no systematic framework]*

VHL is classic: bilateral clear cell RCC, hemangioblastomas of CNS, pancreatic cysts, renal cysts, etc. *[Issue: Brief statement, no detailed reasoning]*

MEN1: pituitary, parathyroid, pancreatic endocrine tumors, but not renal cysts or hemangioblastomas. *[Issue: Superficial elimination - just "but not X"]*

TSC: cortical tubers, subependymal nodules, renal angiomyolipomas, but not hemangioblastomas. *[Issue: Lists features without explaining why they exclude diagnosis]*

PKD: bilateral cystic kidneys, but not brain lesions. *[Issue: One-sentence dismissal]*

HLRCC: renal cell carcinoma (papillary type 2), cutaneous leiomyomas, uterine leiomyomas, but not brain hemangioblastomas. *[Issue: No detailed analysis]*

Thus VHL fits best. The presence of multiple bilateral renal cystic lesions with septations and enhancing lesions suggests clear cell RCC. The brain lesions are hemangioblastomas. Splenic hamartoma is also associated with VHL? *[Issue: Shows uncertainty - questioning itself]* Splenic hamartoma is not classic but can be seen. Pancreatic cysts also seen. So VHL is the best. *[Issue: Lacks confidence and systematic synthesis]*

Base Model Final Answer: Von Hippel-Lindau syndrome (VHL) – CORRECT but with uncertain, superficial reasoning

Fine-Tuned Model Response

Step 1 – Relate the clinical picture to the imaging

The patient is a 41-year-old man with microscopic haematuria, a palpable right-flank mass and recurrent headaches.

The flank mass corresponds to the enlarged, heterogeneous right kidney seen on CT. The headaches are explained by the posterior-fossa lesions on brain MRI, which are cystic-solid, avidly enhancing and causing mass effect on the pons. The combination of renal cystic-solid lesions, pancreatic cysts, splenic vascular anomalies (splenic-vein dilation, pancreatic-splenic collaterals) and multiple posterior-fossa haemangioblastomas is highly suggestive of a hereditary tumour-spectrum disorder.

Step 2 – Map findings to each differential

Differential	Typical imaging/clinical hallmarks	Concordance with this case	Reason for exclusion
Von Hippel-Lindau (VHL)	Bilateral renal cystic-solid lesions (cystic-solid RCC), pancreatic cysts, splenic vascular malformations, multiple cerebellar/brain-stem haemangioblastomas, haematuria, flank mass, headaches.	All key features present; age fits (40-50 yr).	–
Sporadic haemangioblastomas	Usually solitary, no systemic renal or pancreatic lesions.	Multiple haemangioblastomas present; renal and pancreatic findings are absent in sporadic disease.	Multiple haemangioblastomas with systemic findings exclude sporadic form.
MEN-1	Pancreatic neuroendocrine tumours, parathyroid hyperplasia, pituitary adenomas; renal cysts are uncommon, haemangioblastomas are not typical.	Pancreatic cysts are simple, not neuroendocrine; no endocrine lesions reported; renal lesions are cystic-solid RCC, not typical MEN-1.	Absence of neuroendocrine tumours and endocrine dysfunction.
TSC	Multiple cortical tubers, subependymal nodules, renal angiomyolipomas (fat-dense), cardiac rhabdomyomas, retinal hamartomas.	No cortical tubers, no fat-dense renal lesions, no cardiac or retinal findings.	Pathognomonic TSC features (cortical tubers, angiomyolipomas) are absent.
PKD	Bilateral, large, non-enhancing cysts; no solid enhancing components; no pancreatic or splenic vascular lesions; no brain haemangioblastomas.	Renal lesions are cystic-solid with necrotic centres, not simple cysts; extra-renal lesions present.	Presence of solid enhancing components and extra-renal manifestations.
HLRCC	Renal cell carcinoma (often papillary type II) with aggressive behaviour; no pancreatic cysts or splenic vascular anomalies; no haemangioblastomas.	Renal lesions are cystic-solid but lack the classic papillary-type II morphology; extra-renal findings are absent in HLRCC.	Missing characteristic HLRCC features (aggressive papillary RCC, cutaneous leiomyomas).

Step 3 – Systematic elimination

- Sporadic haemangioblastomas are excluded because the patient has multiple CNS lesions accompanied by systemic renal and pancreatic manifestations, which are not seen in sporadic cases.
- MEN-1 is ruled out by the absence of neuroendocrine pancreatic tumours, parathyroid disease, or pituitary adenomas.
- TSC is eliminated by the absence of cortical tubers, subependymal nodules, and fat-dense angiomyolipomas.
- PKD is excluded because the renal lesions are cystic-solid with enhancing components and necrotic centres, not simple non-enhancing cysts.
- HLRCC is ruled out by the lack of aggressive papillary-type II RCC morphology and the presence of CNS haemangioblastomas, which are not part of HLRCC.
- **Only VHL accounts for the complete constellation of findings** : bilateral cystic-solid renal lesions, pancreatic cysts, splenic vascular anomalies, and multiple CNS haemangioblastomas.

Step 4 – Converge on the final diagnosis

The presence of bilateral cystic-solid renal lesions with necrotic centres, multiple simple pancreatic cysts, splenic vascular dilatation, and multiple posterior-fossa haemangioblastomas together with haematuria and a flank mass fits the classic VHL phenotype. None of the other entities account for the full spectrum of findings. The logical synthesis of clinical presentation and imaging demonstrates that the patient's findings are most consistent with Von Hippel-Lindau syndrome. Genetic confirmation (VHL gene mutation) would be the next step, followed by multidisciplinary surveillance for renal, pancreatic, splenic, and CNS manifestations.

Fine-Tuned Model Final Answer: Von Hippel-Lindau syndrome (VHL) – CORRECT with systematic, confident

reasoning

Key Improvements from Fine-Tuning:

- **Structured framework:** Transformed unstructured list into systematic 4-step analysis with explicit clinical-imaging correlation
- **Comprehensive comparison:** Added detailed 6-syndrome table with concordance/discordance columns vs. brief text dismissals
- **Multi-system integration:** Step 1 explicitly synthesizes renal, pancreatic, splenic, and CNS findings into hereditary tumor syndrome pattern
- **Explicit elimination logic:** "Reason for exclusion" column with pathophysiologic justification vs. superficial "but not X" statements
- **Eliminated uncertainty:** Definitive statements about splenic findings vs. questioning ("Splenic hamartoma is also associated with VHL?")
- **Clinical confidence:** Comprehensive synthesis with next-step recommendations vs. tentative conclusion

Case Study

Case Study 2: Primary Cardiac Lymphoma

Case Presentation

Clinical History: An 81-year-old male with a history of paroxysmal atrial fibrillation presents to the emergency department with a one-week onset of orthopnoea and exertional dyspnoea. Laboratory tests demonstrate elevated troponins, the electrocardiogram reveals a third-degree atrioventricular block, and the echocardiogram shows right ventricular thickening and pericardial effusion.

Imaging Findings: A PET-CT scan was carried out revealing a large hypermetabolic myocardial tissue. It extended through the right chambers and around the large vessels, sparing the left ventricle. Additionally, a hypermetabolic nodular image was identified at the left lung base. Therefore, a contrast-enhanced chest CT scan was performed. It confirmed the presence of an infiltrative hypodense mass in the myocardium. It involved the right atrium, right ventricle, interatrial septum, and atrioventricular groove. The mass caused mural thickening of the right cavities. A cuff encircled the right coronary artery along its course. A moderate pericardial effusion was also observed. Finally, the CT scan confirmed the solid nodule in the posterior segment of the left lower lobe. A CT-guided percutaneous biopsy of the lung nodule was made for histological examination.

Differential diagnoses to consider: Angiosarcoma, IgG4-related disease, Primary cardiac lymphoma, Erdheim-Chester disease, Undifferentiated pleomorphic sarcoma

Ground Truth: Primary cardiac lymphoma

Base Model Response (Before Fine-Tuning)

We need to reason step by step using only provided info. The case: 81-year-old male, paroxysmal atrial fibrillation, orthopnoea, exertional dyspnoea, elevated troponins, ECG shows third-degree AV block, echo shows right ventricular thickening and pericardial effusion. PET-CT shows large hypermetabolic myocardial tissue extending through right chambers and around large vessels, sparing left ventricle. Hypermetabolic nodular image at left lung base. Contrast CT confirms infiltrative hypodense mass in myocardium involving right atrium, right ventricle, interatrial septum, AV groove. Mural thickening of right cavities. Cuff around right coronary artery. Moderate pericardial effusion. Solid nodule in posterior segment left lower lobe. *[Issue: Just lists findings without synthesis]*

Let's analyze each:

Angiosarcoma: Primary cardiac sarcoma, most common primary malignant tumor of heart. Usually involves right atrium, can extend to right ventricle, pericardial effusion, can cause arrhythmias, conduction block. PET hypermetabolic. Age: typically younger (median 40-50). But can occur in older. *[Issue: Makes excuses instead of using age as exclusion criterion]* Lung metastasis possible. So fits. *[Issue: Prematurely accepts this diagnosis]*

IgG4-related disease: Infiltrative disease, can involve heart (IgG4-related pericarditis, myocarditis). Usually involves pericardium, can cause thickening, but not typically hypermetabolic mass on PET? Could show uptake. But IgG4 disease often involves multiple organs, but lung involvement can be nodules. However, IgG4 disease rarely presents as a large infiltrative mass in myocardium. Also would have elevated IgG4 levels, histology with IgG4 plasma cells. Not typical. [Issue: Rambling, uncertain reasoning]

Primary cardiac lymphoma: Rare, often involves right atrium, can cause conduction block, pericardial effusion, infiltration. PET hypermetabolic. Age: can be older. Lung involvement? Usually no lung nodules. But could metastasize to lung. But primary cardiac lymphoma often involves both atria and ventricles, but can be localized. Could present with AV block. So possible. [Issue: Doesn't recognize AV block as KEY feature for lymphoma]

Erdheim-Chester disease: Non-Langerhans cell histiocytosis, systemic infiltration, can involve heart (pericardial thickening, infiltration of myocardium). Usually involves both ventricles, but can involve right side. Also can involve lungs (nodules). Age: older adults. PET hypermetabolic. But typical features: symmetric osteosclerosis of long bones, retroperitoneal fibrosis, etc. Not mentioned. Also infiltration often involves both ventricles, not sparing left ventricle. So less likely. [Issue: Superficial elimination]

Undifferentiated pleomorphic sarcoma: A type of sarcoma, but not typical for heart. Could be primary cardiac sarcoma but usually angiosarcoma is most common. Undifferentiated pleomorphic sarcoma can be in heart but less common. Could present similarly. But the mass is hypermetabolic, infiltration of right chambers. Could be. [Issue: No real elimination logic]

We need to choose the most likely. The key features: right atrium/ventricle involvement, pericardial effusion, conduction block, hypermetabolic mass, lung nodule. Angiosarcoma is classic for right atrium, pericardial effusion, conduction block, metastasis to lung. [Issue: Misses that AV block is MORE classic for lymphoma] Primary cardiac lymphoma also can present similarly. But which is more likely? Let's consider age: 81. Angiosarcoma usually younger. Primary cardiac lymphoma often in immunocompromised or older? Primary cardiac lymphoma can occur in older adults. But the presence of a lung nodule that was biopsied: likely metastasis. In angiosarcoma, lung metastases common. In primary cardiac lymphoma, metastasis to lung less common? Actually lymphoma can metastasize to lung. But the lung nodule is hypermetabolic. The biopsy would reveal histology. But we don't have histology results. [Issue: Circular reasoning without clear conclusion]

Angiosarcoma often shows infiltrative mass in right atrium, can extend to right ventricle, pericardial effusion, can encircle coronary arteries. The mass can be hypermetabolic. The left ventricle is spared. That fits. Primary cardiac lymphoma often involves both atria and ventricles, but can be localized. But the mass in this case is large, infiltrative, hypermetabolic, involving right atrium, right ventricle, interatrial septum, AV groove. That is typical for angiosarcoma. Also the presence of a lung nodule suggests metastasis. So angiosarcoma is likely. [Issue: Wrong conclusion - prioritized lung nodule over AV block]

Base Model Final Answer: Angiosarcoma – INCORRECT

Fine-Tuned Model Response

Step 1 – Relate the clinical picture to the imaging

The patient is an elderly man with new-onset orthopnoea, exertional dyspnoea, a third-degree AV block, elevated troponin and a right-ventricular-predominant thickening on echo.

These findings point to a process that involves the right-sided myocardium, the conduction system (AV node) and produces a pericardial effusion. The PET-CT shows a large, intensely FDG-avid mass that surrounds the right atrium, right ventricle, inter-atrial septum and the atrioventricular groove, sparing the left ventricle. A second hypermetabolic nodule is seen in the left lower-lobe lung, later confirmed as a metastatic lesion. Thus we have a right-sided cardiac infiltrative tumour with extra-cardiac metastasis.

Step 2 – Map findings to each differential

Differential	Typical imaging & clinical features	Concordance with this case	Discordance
Primary cardiac lymphoma (PCL)	Usually involves right-sided chambers, encases AV node → AV block; often presents with pericardial effusion; may be FDG-avid; can metastasize to lung; left ventricle usually spared.	All three hallmarks present (right-sided infiltrate, AV block, pericardial effusion, lung metastasis, FDG avidity).	None.
Angiosarcoma	Most common primary cardiac sarcoma; tends to involve right atrium, may cause hemopericardium, pericardial effusion; often shows heterogeneous enhancement, necrosis, and may invade coronary arteries.	Right-sided location and pericardial effusion fit.	Angiosarcoma usually shows a more heterogeneous, necrotic mass with prominent vascular channels; the PET-CT shows a uniformly hypermetabolic, well-circumscribed infiltrate, and the mass encircles the right coronary artery without obvious necrosis. Metastasis to lung is possible but less common than lymphoma.
IgG4-related disease	Can cause "tumefactive" cardiac lesions, but typically presents with systemic features (pancreatitis, retro-orbital disease), and imaging shows diffuse myocardial thickening rather than a discrete mass; PET may be mildly FDG-avid.	None of the systemic IgG4 manifestations are present.	Lack of extra-cardiac IgG4-related lesions and the aggressive, FDG-avid nature argue against it.
Erdheim-Chester disease	Bilateral symmetric osteosclerosis of long bones, pericardial thickening, retro-orbital pseudotumor; cardiac involvement is usually infiltrative but not as focal; PET may be positive.	No bone lesions or other classic sites.	Unlikely.
Undifferentiated pleomorphic sarcoma	Rare, often involves left ventricle, may be large, heterogeneous, necrotic, and can cause hemopericardium.	Right-sided location is atypical; mass is uniformly hypermetabolic without necrosis.	Unlikely.

Step 3 – Systematic elimination

- Angiosarcoma is less likely because the lesion is uniformly FDG-avid, lacks necrotic areas, and the patient's age (81) is above the typical 30-50 yr range.
- IgG4-related disease and Erdheim-Chester disease are excluded by the absence of systemic manifestations and characteristic extra-cardiac findings.
- Undifferentiated pleomorphic sarcoma is improbable given the right-sided predominance and lack of necrosis.

Step 4 – Converge on the most plausible diagnosis

The combination of (1) right-sided cardiac infiltration with AV node encasement causing complete heart block, (2) moderate pericardial effusion, (3) intense FDG uptake, (4) a solitary lung metastasis, and (5) the patient's age and clinical course, aligns perfectly with primary cardiac lymphoma. The subsequent CT-guided lung biopsy confirming metastatic lymphoma clinches the diagnosis.

Fine-Tuned Model Final Answer: Primary cardiac lymphoma – CORRECT

Key Improvements from Fine-Tuning:

- Recognized key clinical feature:** Immediately identified AV node encasement causing third-degree AV block as

pathognomonic for primary cardiac lymphoma

- **Systematic framework:** Transformed rambling analysis into structured 4-step approach with clear clinical synthesis
- **Detailed differential table:** Added comprehensive 5-entity comparison with concordance/discordance analysis vs. unstructured text
- **Proper age weighting:** Used patient age (81 years) to definitively exclude angiosarcoma (typical 30-50 yr) rather than making excuses
- **Imaging pattern recognition:** Identified "uniformly hypermetabolic, well-circumscribed" pattern as distinguishing from heterogeneous, necrotic angiosarcoma
- **Clinical correlation:** Step 4 synthesizes all findings (AV block + location + effusion + lung met + age) to converge on correct diagnosis

Case Study

Case Study 3: Non-Ischemic Cerebral Enhancing (NICE) Lesions

Case Presentation

Clinical History: Five days after an uncomplicated embolisation of an asymptomatic, growing right middle cerebral artery (MCA) aneurysm, a 56-year-old woman comes to the ER due to headache, a seizure and fluctuant left upper extremity weakness and left campimetric defects. A Todd's paralysis is suspected, and the patient is admitted for a workup.

Imaging Findings: Initially, a brain CT is performed, which shows no significant abnormalities apart from the embolisation material. Then a brain MRI is performed, including the following sequences: DWI, SWI, T2, FLAIR, 3D TOF and pre and post-gadolinium T1. The MRI discloses multiple round lesions varying in size in the right hemisphere. The lesions are spontaneously T1 hypointense and T2 hyperintense, the largest ones showing a small, central T2 hypointensity. Post-gadolinium enhancement is demonstrated in all the lesions. No restricted diffusion or susceptibility artefacts are present. Follow-up imaging after 6 months shows overall improvement with resolution of the enhancing foci. However, T2 hyperintensity is still present, and central punctate susceptibility artefacts have appeared, interpreted as microhaemorrhagic foci.

Differential diagnoses to consider: Non-ischemic cerebral enhancing (NICE) lesions, Subacute cerebral infarcts, Cerebral microabscesses, Brain metastases

Ground Truth: Non-ischemic cerebral enhancing (NICE) lesions

Base Model Response (Before Fine-Tuning)

We need to consider the imaging features: multiple round lesions, T1 hypointense, T2 hyperintense, central T2 hypointensity, post-gadolinium enhancement, no diffusion restriction, no susceptibility artifacts initially. After 6 months, resolution of enhancement, persistent T2 hyperintensity, central punctate susceptibility artifacts (microhemorrhages). *[Issue: Lists features without prioritizing temporal context]*

This suggests that the lesions were likely embolization-related changes: e.g., embolic microinfarcts? But no diffusion restriction. *[Issue: Immediately questions own reasoning]* Subacute infarcts would show diffusion restriction early, then T2 hyperintensity, then resolution of enhancement? But subacute infarcts usually show restricted diffusion early, then T2 hyperintensity, then no enhancement. But here no diffusion restriction. *[Issue: Circular reasoning]* Also multiple lesions after embolization could be due to embolic microinfarcts from procedure. But the lesions are enhancing, which is not typical for infarcts. However, early subacute infarcts can show enhancement due to breakdown of BBB. But they usually show diffusion restriction early. But maybe small lesions might not show diffusion restriction? *[Issue: Making excuses for contradictory evidence instead of using it to exclude]* But central T2 hypointensity suggests hemorrhagic component? But no susceptibility artifacts initially. After 6 months, microhemorrhages appear. Could be due to microinfarcts with hemorrhagic transformation? But microhemorrhages appear later. *[Issue: Continued circular reasoning]*

Alternatively, could be cerebral microabscesses? They would show diffusion restriction, rim enhancement, central T2 hyperintensity. But no diffusion restriction. So unlikely.

Brain metastases: multiple enhancing lesions, T1 hypointense, T2 hyperintense, central T2 hypointensity? Usually metastases have ring enhancement, central necrosis, sometimes hemorrhage. But metastases would show diffusion restriction? Not necessarily. But metastases would not spontaneously resolve after 6 months unless treated. Also patient had no known primary cancer. So less likely.

Non-ischemic cerebral enhancing (NICE) lesions: This is a broad category. [Issue: Dismisses correct answer as "too broad"] Could include inflammatory lesions, demyelinating lesions, etc. But the context of embolization suggests procedure-related changes. Could be "post-embolization changes" like "cerebral embolic infarcts" or "cerebral microinfarcts" that enhance due to BBB breakdown. The resolution of enhancement over 6 months fits with healing of infarcts. The persistent T2 hyperintensity indicates gliosis or chronic changes. The microhemorrhages appear later due to microinfarcts with hemorrhagic transformation. [Issue: Talks around NICE but doesn't recognize it as specific diagnosis]

Thus the most likely is Subacute cerebral infarcts. [Issue: Wrong conclusion - failed to use absence of DWI restriction as definitive exclusion criterion]

Base Model Final Answer: Subacute cerebral infarcts – INCORRECT

Fine-Tuned Model Response

Step 1 – Relate the clinical picture to the imaging problem

The patient had a recent endovascular embolisation of a right MCA aneurysm. Five days later she develops a new headache, a focal seizure and transient left-sided weakness with visual field loss. This post-intervention presentation with focal neurological deficits immediately suggests a complication rather than a primary neoplasm or infection. The transient weakness is classic for Todd's paralysis, which is a post-ictal phenomenon that can mimic a new infarct.

Step 2 – Describe the MRI pattern and map to differentials

MRI Pattern:

- Multiple round foci confined to the right cerebral hemisphere (the side of the intervention).
- Spontaneous T1-hypointensity, T2-hyperintensity, with a small central T2-hypointense core.
- Uniform, homogeneous post-gadolinium enhancement in all lesions.
- No diffusion restriction on DWI, no blooming on SWI at the initial scan.
- Follow-up (6 mo) shows resolution of enhancement, persistent T2 hyperintensity, and new tiny susceptibility foci (micro-haemorrhages).

This pattern is characteristic of NICE lesions: they are multiple, well-circumscribed, enhance avidly, lack diffusion restriction, and evolve to a non-enhancing T2-hyperintense state with occasional micro-bleeds.

Differential	Expected imaging features	Concordance/discordance with case
NICE (post-embolisation)	Multiple, round, enhancing lesions confined to the ipsilateral hemisphere; no diffusion restriction; may show central T2 hypointensity; evolution to non-enhancing T2 hyperintensity with micro-bleeds.	All criteria met: multiple right-hemisphere lesions, homogeneous enhancement, no DWI restriction, central T2 core, evolution pattern.
Subacute cerebral infarcts	Usually wedge-shaped, follow vascular territories; diffusion restriction present in the acute/subacute phase; may show blooming on SWI due to haemorrhagic conversion; enhancement is often peripheral and delayed.	Lesions are round, not territorial; no diffusion restriction; no SWI blooming initially; enhancement is uniform, not peripheral.
Cerebral microabscesses	Often solitary or few, ring-enhancing with central diffusion restriction; may have surrounding oedema; SWI may show central susceptibility.	Multiple lesions, no diffusion restriction, no oedema, uniform rather than ring enhancement.
Brain metastases	Usually multiple, often peripherally located, may have surrounding oedema, variable enhancement (often heterogeneous), and frequent susceptibility artefacts from haemorrhage.	Lesions are confined to one hemisphere, lack surrounding oedema, enhancement is homogeneous, and initial SWI is negative.

Step 3 – Systematic elimination

- Subacute infarcts are excluded by the absence of diffusion restriction and the non-territorial, round morphology. Acute ischemic lesions would show restricted diffusion, which is not present here.
- Microabscesses are unlikely because there is no diffusion restriction, no oedema, and the enhancement is not ring-like. Abscesses typically show a hyperintense DWI core.
- Metastases are improbable given the unilateral distribution, lack of perilesional oedema, and the temporal relationship to a recent endovascular procedure. The patient also has no known primary malignancy.
- The combination of a recent aneurysm embolisation, unilateral multiple enhancing lesions without diffusion restriction, central T2 hypointensity, and the characteristic evolution (resolution of enhancement, persistence of T2 hyperintensity, and later micro-bleeds) fits the classic profile of NICE lesions.

Step 4 – Converge on the final diagnosis

The temporal relationship to endovascular intervention is the key clinical clue. The combination of multiple ipsilateral round enhancing lesions without diffusion restriction, the presence of central T2 hypointensity, and the characteristic 6-month evolution (resolution of enhancement with persistent T2 signal and development of microhaemorrhages) is pathognomonic for non-ischemic cerebral enhancing (NICE) lesions. Recognizing this pattern prevents unnecessary invasive workup and guides appropriate follow-up imaging.

Fine-Tuned Model Final Answer: Non-ischemic cerebral enhancing (NICE) lesions – CORRECT

Key Improvements from Fine-Tuning:

- Recognized temporal context:** Immediately identified "5 days post-embolization" as key diagnostic clue for procedural complication (NICE lesions)
- Used absence of DWI restriction definitively:** Applied lack of diffusion restriction to systematically exclude infarcts rather than making excuses
- Eliminated circular reasoning:** Replaced "But maybe..." contradictions with clear exclusion logic based on imaging features
- Recognized NICE as specific diagnosis:** Understood NICE lesions as established post-procedural entity, not just "broad category"
- Applied evolution pattern:** Used 6-month follow-up (resolution of enhancement → persistent T2 → microbleeds) as pathognomonic feature
- Systematic framework:** Transformed rambling analysis into structured 4-step approach with clear MRI pattern description and differential table